Exploiting the centimeter resolution of UAV multispectral imagery to improve remote-sensing estimates of canopy structure and biochemistry in sugar beet crops

Sylvain Jay, Frédéric Baret, Dan Dutartre, Ghislain Malatesta, Stéphanie Héno, Alexis Comar, Marie Weiss, Fabienne Maupas

Exploiting the centimeter resolution of UAV multispectral imagery to improve remote-sensing estimates of canopy structure and biochemistry in sugar beet crops

Sylvain Jay[a,*], Frédéric Baret[b], Dan Dutartre[c], Ghislain Malatesta[a], Stéphanie Héno[a], Alexis Comar[c], Marie Weiss[b], Fabienne Maupas[a]

[a] *Institut Technique de la Betterave, 45 rue de Naples, 75008 Paris, France*
[b] *INRA UMR 114 EMMAH, UMT CAPTE, Domaine Saint-Paul, Site Agroparc, F-84914 Avignon, France*
[c] *HIPHEN SAS, 22b rue Charrue, 84000 Avignon, France*

Abstract

The recent emergence of unmanned aerial vehicles (UAV) has opened a new horizon in vegetation remote sensing, especially for agricultural applications. However, the benefits of UAV centimeter-scale imagery are still unclear compared to coarser resolution data acquired from satellites or aircrafts. This study aims (i) to propose novel methods for retrieving canopy variables from UAV multispectral observations, and (ii) to investigate to what extent the use of such centimeter-scale imagery makes it possible to improve the estimation of leaf and canopy variables in sugar beet crops (*Beta Vulgaris* L.). Five important structural and biochemical plant traits are considered: green fraction (GF), green area index (GAI), leaf chlorophyll content (C_{ab}), as well as canopy chlorophyll (CCC) and nitrogen (CNC) contents.

Based on a comprehensive data set encompassing a large variability in canopy structure and biochemistry, the results obtained for every targeted trait demonstrate the superiority of centimeter-resolution methods over two standard remote-sensing approaches (i.e., vegetation indices and PROSAIL inversion) applied to average canopy reflectances. Two variables (denoted $GF_{GREENPIX}$ and VI_{CAB}) extracted from the images are shown to play a major role in these performances. $GF_{GREENPIX}$ is the GF estimate obtained by thresholding the Visible Atmospherically Resistant Index ($VARI$) image, and is shown to be an accurate and robust (e.g., against variable illumination conditions) proxy of the structure of sugar beet canopies, i.e., GF and GAI. VI_{CAB} is the mND_{blue} index value averaged over the darkest green pixels, and provides critical information on C_{ab}. When exploited within uni- or multivariate empirical models, these two variables improve the GF, GAI, C_{ab}, CCC and CNC estimates obtained with standard approaches, with gains in estimation accuracy of 24, 8, 26, 37 and 8 %, respectively. For example, the best CCC estimates ($R^2 = 0.90$) are obtained by multiplying C_{ab} and GAI estimates respectively derived from VI_{CAB} and a log-transformed version of $GF_{GREENPIX}$, log(1-$GF_{GREENPIX}$).

The $GF_{GREENPIX}$ and VI_{CAB} variables, which are only accessible from centimeter-scale imagery, contributes to a better identification of the effects of canopy structure and leaf biochemistry, whose influences may be confounded when considering coarser resolution observations. Such results emphasize the strong benefits of centimeter-scale UAV imagery over satellite or airborne remote sensing, and demonstrate the relevance of low-cost multispectral cameras to retrieve a number of plant traits, e.g., for agricultural applications.

Keywords: Chlorophyll content, Field phenotyping, Green fraction, Green area index, Nitrogen content, Remote sensing, Sugar beet, UAV.

1. Introduction

Non-destructive and timely monitoring of crop structural and biochemical traits is of major importance to assess the physiological and phenological status of the plants and to further understand their functioning over time. A number of applications benefit from such an accurate monitoring, including (i) precision agriculture, which aims to adapt cultural practices to the actual state of the canopy over space and time (McBratney et al., 2005; Zhang and Kovacs, 2012), and (ii) plant phenotyping, which aims to identify the genetic basis of important traits controlling yield and quality (Furbank and Tester, 2011; Sankaran et al., 2015; Zaman-Allah et al., 2015).

Some of the most relevant crop structural and biochemical traits to be monitored characterize the efficiency with which light, water and nutrients are captured and used for biomass production and yield (Araus and Cairns, 2014). Since the green area index (GAI) and the green fraction (GF) closely relate to the capability of the crop to intercept the incoming photosynthetically-active radiation (PAR), they are both key variables for photosynthesis, respiration and evapotranspiration (Verger et al., 2014). GAI and GF are also good proxies of biomass as well as good indicators of developmental stages and various abiotic and biotic stresses (Yang et al., 2017). For all these reasons, GAI is considered as an essential state variable for crop modeling (Baret et al., 2007; Clevers, 1997; Dong et al., 2017; Dorigo et al., 2007; Launay and Guerif, 2005). In addition to these structural variables, knowledge of leaf chlorophyll content (C_{ab}) provides critical information on the capability of the crop to absorb the intercepted PAR and to produce biomass (Gitelson et al., 2005; Houborg et al., 2015). C_{ab} is also a proxy of nitrogen content (Schlemmer et al., 2013) and maximum rate of carboxylation (Croft et al., 2017; Houborg et al., 2015). Changes in C_{ab} can also be related to nutrient stresses and developmental stages (Gitelson et al., 2005). By upscaling C_{ab} to the canopy level, thus considering the canopy chlorophyll content (CCC), it is possible to assess the total canopy-scale productivity of the crop (Gitelson et al., 2006b; Inoue et al., 2016). As CCC is also an accurate proxy of canopy nitrogen content (CNC) (Baret et al., 2007; Jay et al., 2017b; Schlemmer et al., 2013), it is therefore a critical variable for many agricultural applications.

Optical sensors embedded on ground-based platforms, aircrafts and satellites have long been used for vegetation monitoring. Indeed, because the canopy structure and biochemistry strongly affect the reflected solar radiation in the optical domain (Jacquemoud and Baret, 1990; Verhoef, 1984), they can potentially be retrieved from the canopy reflectance measured from remote sensing. However, satellite or aerial remote-sensing imagery generally lacks spatial resolution to observe single microplots of a few dozen square meters in the context of field phenotyping (Gago et al., 2015; Sankaran et al., 2015; Yang et al., 2017; Zaman-Allah et al., 2015). Further, the revisit frequency combined with possible cloud occurrence limit the use of satellites for agricultural applications, when observations need to be completed over short critical periods (Inoue et al., 2012; Launay and Guerif, 2005). Possible alternatives to satellites and aircrafts include a variety of ground-based platforms, such as towers (Hilker et al., 2011) or “phenomobiles” (Araus and Cairns, 2014; Busemeyer et al., 2013; Comar et al., 2012; Deery et al., 2014). However, these platforms are limited by their spatial coverage and the difficulty in transporting them from one location to another (Gago et al., 2015; Sankaran et al., 2015; Yang et al., 2017).

Unmanned Aerial Vehicles (UAVs) offer a very attractive alternative : they can be operated conveniently and offer high spatial and temporal resolutions as well as a reasonable spatial coverage (Gago et al., 2015; Sankaran et al., 2015; Van Der Meij et al., 2017; Verger et al., 2014; Zaman-Allah et al., 2015; Zarco-Tejada et al., 2013). Interestingly, the high spatial resolution of UAV data makes it possible to document the within-microplot variability in field phenotyping experiments (Araus and Cairns, 2014; Zaman-Allah et al., 2015). For all of these reasons, UAVs are currently becoming appealing tools for crop monitoring (e.g., Aasen et al., 2015; Domingues Franceschini et al., 2017; Duan et al., 2014; Jin et al., 2017; Van Der Meij et al., 2017; Verger et al., 2014; Zarco-Tejada et al., 2013; Zhou et al., 2017).

Despite this success, the benefits of using the fine spatial resolution accessible from UAV imagery for retrieving the above-mentioned structural and biochemical crop traits have not been clearly quantified yet. The possibility to remove soil and shadow pixels is likely to improve the estimation of leaf biochemistry (Jay et al., 2017a; Moorthy et al., 2008; Zarco-Tejada et al., 2004, 2013, 2001). However, there still lacks methods that take full advantage of the centimeter resolution to improve estimates of canopy variables.

Therefore, the objectives of this study are (i) to propose novel methods for retrieving canopy variables in sugar beet (*Beta Vulgaris* L.) crops using centimeter-scale multispectral imagery, and (ii) to investigate to what extent the use of centimeter-scale imagery makes it possible to improve the estimation of GF, GAI, C_{ab}, CCC and CNC in sugar beet crops at the microplot level. Using an extensive two-year multi-site field experiment, several variables are extracted from UAV multispectral images of microplots, including VI values computed over various subsets of pixels, or GF estimates obtained by thresholding pixel-level VI values. These variables are directly related to the targeted traits, or combined, e.g., within Multiple Linear Regression (MLR) models. These methods are compared to two standard remote-sensing approaches used with coarser resolution data, i.e., Vegetation Indices (VIs) and PROSAIL inversion (Baret et al., 1992; Jacquemoud et al., 2009) applied to the averaged reflectances of microplots. Note that this study follows our previous studies based on ground measurements (Jay et al., 2017b, 2017a), upscaling the results to UAV observations in the perspective of high-throughput field phenotyping and precision agriculture.

2. Materials and methods

2.1. Field experiments

Field experiments were conducted in France during the 2016 and 2017 growing seasons. Four sites with different soil properties (sandy loam for Barenton, calcareous loam for St-Memmie, chalk for Charmont and clay loam for Nizy) were considered (Table 1 and Fig. 1). For each site, one to three trial(s) were monitored. Each trial was organized as a randomized complete block design using a factorial arrangement of various nitrogen fertilizations and/or cultivars and/or plant densities. The microplots were 7 to 10 m long and encompassed four to twelve rows, with 45 cm row spacing and 16 to 18 cm plant spacing. In total, fourteen cultivars, eight nitrogen fertilization and seven plant densities were considered over the two years and under various soil and weather conditions, resulting in 274 microplots available.

Table 1 : Summary of field experiments.

Year	Trial	Soil	Plant density (plants/m²)	Nitrogen rate (kgN/ha)	Cultivar Id.	Number of microplots	Number of replicates	Date	Number of reference measurements				
									GF	GAI	C_{ab}	CCC	CNC
2016	Barenton 1	Sandy loam	11.5	0; 100; 150	1-4	36	6	05/24	36	18	18	6	18
								06/06	36	12	18	6	18
								06/23	36	18	18	6	18
								07/04	36	N/A	18	N/A	18
								07/21	N/A	18	18	6	18
	Barenton 2	Sandy loam	7; 10; 14	0; 100; 150	5-13	11	1	06/06	11	11	11	11	N/A
								06/22	11	11	10	10	N/A
	StMemmie 1	Calcareous loam	11	40; 80; 120	1-4	12	2	06/07	12	12	12	12	N/A
	StMemmie 2	Calcareous loam	7; 10; 14	40; 80; 120	5-13	11	1	06/07	11	11	11	11	N/A
2017	StMemmie 3	Calcareous loam	10	0; 40; 80	14	6	2	07/04	6	6	6	6	N/A
								07/17	6	5	6	5	N/A
	Charmont	Chalk	10.5	0; 70; 110; 150	14	4	1	07/04	4	4	4	4	N/A
								07/21	4	4	4	4	N/A
	Nizy	Clay loam	9.5	0; 40; 80	1-4	29	5	07/19	29	5	23	5	24

2.2. GF, GAI, C_{ab}, CCC and CNC reference measurements

For each microplot, the proportion of green pixels as observed from nadir, GF (unitless), was estimated from millimeter-scale RGB imagery using Support Vector Machine (SVM) classification (Vapnik and Vapnik, 1998) to identify green pixels (see section 2.4.1).

GAI (unitless) was estimated based on five hemispherical photographs acquired with a digital camera positioned above a representative part of the canopy. The CAN-EYE freeware (http://www6.paca.inra.fr/can-eye/) was then used to retrieve the effective GAI (Weiss et al., 2004) from these photographs. Comparison with destructive GAI measurements (see Jay et al. (2017b) for more details about the measurement procedure) over twenty samples with GAI values ranging from 0.15 to 3.00, showed an error of 0.12, thus confirming the strong accuracy of this indirect method (Demarez et al., 2008).

The mean C_{ab} (in µg/cm²) value of each microplot was estimated using a Dualex scientific+^{TM} leafclip (Force-A, Orsay, France). After selecting six plants representative of the microplot in terms of color and plant structure, five measurements per plant were performed at different shoot levels to account for the within-plant variability. The thirty Dualex readings obtained for each microplot were converted into actual C_{ab} values using the relationship provided by Cerovic et al. (2012) for dicotyledons to account for saturation occurring for high C_{ab} values (Jay et al., 2016). Finally, the thirty C_{ab} values were averaged to obtain a single C_{ab} value for each microplot.

For each microplot, CCC (in g/m²) was computed as the product of GAI and C_{ab} (Baret et al., 2007; Jacquemoud et al., 1995).

CNC was measured destructively after image acquisition. For this purpose, ten plants representative of each microplot and corresponding to a 1 m² area, were harvested. Leaves were placed in an oven at 75°C until their weight stabilized, and their dry mass was measured. The average leaf nitrogen concentration (in % of dry mass) was measured using the Dumas method (Dumas, 1831). CNC (in g/m²) was then determined by multiplying leaf nitrogen concentration by dry mass per unit soil area.

The ground-based measurements of GAI, C_{ab} and CNC were performed within two days of the corresponding UAV flight, during which variations of these variables were assumed to be negligible.

Unfortunately, not all the ground variables were measured for each of the 274 sampled microplots (Table 1). In the case of Barenton 1 trial, GAI was only measured for three replicates out of six, while C_{ab} and CNC were measured for the other three replicates. The three C_{ab} and GAI values available were thus averaged to provide a proxy of the average CCC value over the six replicates. Note that GAI was measured for only two replicates on June 6, 2016. Further, GAI was not measured on July 4, 2016, resulting in no CCC values for this date. Finally, GF was not measured for the last date due to full canopy cover. In the case of Nizy trial, C_{ab} and CNC were measured for four replicates out of five, while GAI was measured for the remaining one. The four C_{ab} values available over the four replicates were thus averaged to provide proxies of C_{ab} values and therefore proxies of CCC values for the last replicate with measured GAI. This was justified by the low variability in C_{ab} observed over the four replicates (i.e., standard deviations were lower than 2 µg/cm²). Note that Barenton 1 and Nizy were the only trials where CNC was measured.

2.3. UAV data acquisition

The two cameras used in this study were embedded on a hexacopter (based on Mikrokopter components), and fixed on a two-axis gimbal to point vertically downward. The first camera was a SONY ILCE-5100 digital RGB camera equipped with a 30 mm focal length lens. It was set on speed priority and auto ISO mode, with speed of 1/1000 sec, and acquired 6000 x 4000 pixel images saved in TIFF format.

The second camera was an AIRPHEN multispectral camera (www.hiphen-plant.com/plant-phenotyping/airphen_41.html) equipped with an 8 mm focal length lens and acquiring 1280 x 960 pixel images saved in TIFF format. AIRPHEN is made of six individual cameras equipped with filters centered on 450, 530, 560 (in 2017, the 570 nm band replaced the 560 nm one), 675, 730 and 850 nm, with a spectral resolution of 10 nm. The integration time of each of the six cameras was adjusted automatically to minimize saturation and maximize the dynamics. Both the RGB and the multispectral cameras acquired images continuously at a 1 Hz frequency.

The flight plan was designed to ensure 80% overlap both across- and along-track. The UAV was first flown at 40 m altitude with the RGB camera, corresponding to a 6 mm spatial resolution. The AIRPHEN multispectral camera was then flown at 60 m altitude in 2016 (corresponding to a 2.7 cm spatial resolution), and 35 m altitude in 2017 (corresponding to a 1.6 cm spatial resolution). These resolutions were finer than the minimum resolution of 4 cm recommended by Jay et al. (2017a) for optimal C_{ab} estimation in sugar beet crops.

Radiometric calibration was performed using a 3 m² carpet reference panel, which could conveniently be used in the field while showing adequate radiometric properties. More specifically, the bidirectional reflectance distribution function of this panel was measured in the laboratory similarly as Verger et al. (2014), and showed a nearly Lambertian behavior for viewing zenith angles lower than 30°, and 8 % reflectance for all of the six bands. Note that the low reflectance of the panel was close to that of soil and vegetation (Fig. 7), which improves the dynamics and signal-to-noise ratio of the imagery. For each UAV flight, this panel was placed horizontally on the ground at a distance of 1.5 times the height of the closest microplot in order to limit adjacency effects. In addition to the radiometric reference panel, nine circular panels of 60 cm diameter were placed within the field and used as ground control points (GCPs). The positions of the GCPs were measured with a RTK GPS providing an accuracy of 2 cm. These different panels are shown in Fig. 1.

Fig. 1 : Examples of RGB images acquired from the UAV over three sites showing differences in growth stages, nitrogen fertilizations and soil properties (Table 1). For each image, the rectangular gray panel is the reference panel used for radiometric calibration, while the smaller circular panels are the GCPs used for georeferencing and orthomosaicking.

UAV RGB and multispectral images were generally acquired around solar noon, with an average solar zenith angle between 29° and 55°. Both UAV flights only took a dozen minutes during which illumination was assumed to be stable. The illumination conditions strongly varied across dates of experiments, ranging from a clear blue sky to a fully overcast one.

2.4. Preprocessing of UAV data

For the sake of clarity, the complete preprocessing chain detailed in the next sections is illustrated in Fig. 2. It first consisted in computing the microplot coordinates and estimating the reference GF of each microplot from RGB images (section 2.4.1). Then, the multispectral bands were co-registered, geometrically and radiometrically corrected (section 2.4.2).

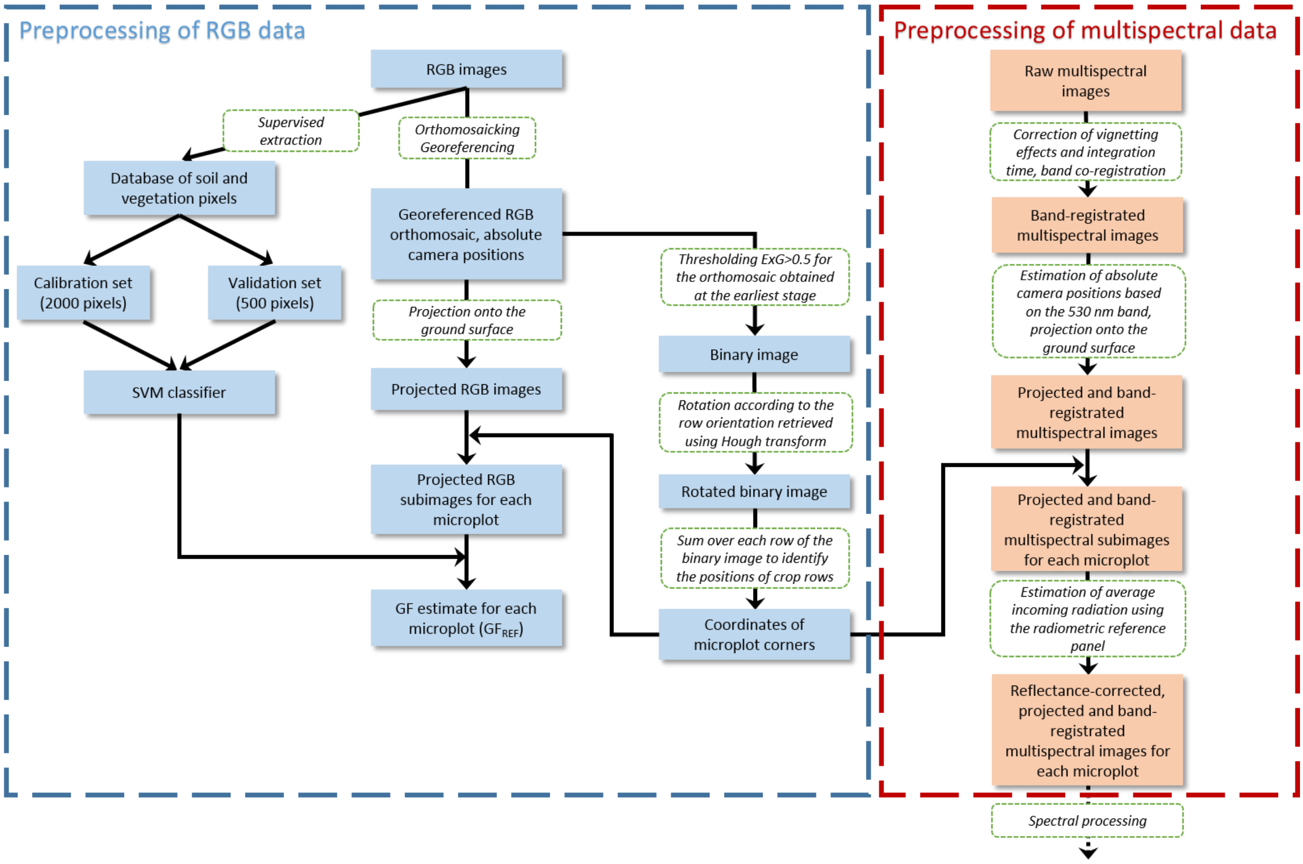

Fig. 2 : Flowchart illustrating the preprocessing of UAV RGB and multispectral images for each trial.

2.4.1. Microplot extraction and GF estimation using RGB images

Agisoft Photoscan Professional edition (Version 1.2.2, Agisoft LLC., Russia) was used to generate an orthomosaic of each trial using the GCPs that were automatically detected. The absolute camera position at the time of each image acquisition was computed, such that each image could be projected onto the ground surface with an accuracy of a few centimeters. For each microplot, 20 to 30 sub-images were then extracted from all the individual projected images containing this microplot. This process ensured a higher image quality as compared to using the orthomosaic (Jin et al., 2017). Note that the microplot coordinates used for sub-image extraction had been automatically computed from the RGB orthomosaic derived from the first flight when the rows were clearly visible, similarly as Jin et al. (2017) to identify the rows and thanks to the knowledge of microplot dimensions and number of rows.

Since the rough classification based on the thresholding of the Excess Green Index (Woebbecke et al., 1995) image was sufficient to identify the rows (Fig. 2), but showed limitations to accurately estimate GF (Jay et al., 2015; Lati et al., 2013), a SVM classifier was trained to classify the RGB images. A database of 2500 soil and vegetation pixels was built, encompassing a large variability in crop state and illumination conditions. This database was randomly split into 2000 pixels used for training and 500 pixels used for validation. The trained SVM classifier showed an overall accuracy better than 95% on the validation set and was then applied to each sub-image to derive the corresponding GF. Among all the sub-images available for each microplot, the five ones showing no saturation and no blur, the closest viewing angles from nadir, and full coverage of the microplot, were selected. The GF estimate of each microplot was finally computed as the average GF over the five selected sub-images. This GF value is considered as the reference one and denoted GF_{REF} in this paper.

2.4.2. Preprocessing of multispectral images for spectral analysis

The six bands were co-registered with an accuracy generally finer than one pixel using the algorithm proposed by Rabatel and Labbé (2016). A master band (530 nm) was then used within Agisoft Photoscan Professional edition (Version 1.2.2, Agisoft LLC., Russia) to derive the camera position for each image acquisition, to project the image onto the ground, and to extract the sub-images corresponding to each microplot in the same way as for RGB imagery. Finally, for each microplot, only sub-images with viewing zenith angles lower than 10° were kept for further analysis to limit bidirectional effects.

For each image, the digital number (DN) value for each pixel (x, y) of the i^{th} band (noted $DN^i(x, y)$) was transformed into a bidirectional reflectance factor value (noted $BRF^i(x, y)$) according to Verger et al. (2014):

$$BRF^i(x,y) = \left(\frac{DN^i(x,y).v^i(x,y)}{t^i}\right).\left(\frac{t^i_{ref}}{\overline{DN^i_{ref}v^i}}\right).BRF^i_{ref} \quad (1)$$

where t^i and t^i_{ref} are, respectively, the integration times of the images acquired over the target and the reference panel, v^i the vignetting matrix used to compensate for the darkening observed in the image corners, $\overline{DN^i_{ref}v^i}$ the pixel-averaged and vignetting-corrected DN value observed over the reference panel of known BRF value BRF^i_{ref}. Note that, similarly to BRF^i_{ref}(section 2.3), v^i was measured in the laboratory as described by Verger et al. (2014). All the sub-images containing the reference panel and acquired with viewing zenith angles lower than 30° were used to get a median value of the $\left(\overline{DN^i_{ref}v^i}/\ t^i_{ref}\right)$ term in Eq. (1). Note that the radiometric calibration process assumes that the illumination conditions are stable during the flight, which was generally the case.

2.5. Approaches used to estimate leaf and canopy variables from UAV multispectral imagery

In this study, five methods exploiting the centimeter spatial resolution of UAV observations are proposed for the estimation of the five targeted plant traits (Table 2 and Fig. 3). These methods rely on the calibration of statistical relationships between each plant trait and one or two VI-based input variable(s) computed from UAV images. Three of these methods (#Avg(VI_AllPix), #Frac(GreenPix) and #Avg(VI_GreenPix)) mainly differ in the set of pixels used to compute the VIs, and the way the VI values are used. The other two methods (#GAI.C_{ab} and #MLR) combine the results obtained with the first three methods. Note that the five variables cannot be estimated with every method (Table 2). The VIs used are first presented in section 2.5.1. Then, the five methods designed for centimeter-scale data as well as the two standard remote-sensing approaches (#RTMI and #VI(Avg_Refl)) serving as baselines for the assessment of the proposed methods are described in sections 2.5.2 and 2.5.3, respectively.

Table 2: Methods used to estimate GF, GAI, C_{ab}, CCC and CNC from UAV multispectral images of microplots. $GF_{GREENPIX}$ is the best GF estimate obtained with approach #Frac(GreenPix), and VI_{CAB} is the VI value that is computed with #Avg(VI_GreenPix) and that is the most correlated with C_{ab}.

Spatial resolution	Approach	Description	GF	GAI	C_{ab}	CCC	CNC
Low	#RTMI	Radiative Transfer Model Inversion using PROSAIL.	✓	✓	✓	✓	-
	#VI(Avg_Refl)	VI computed from average microplot reflectance.	✓	✓	✓	✓	✓
High	#Avg(VI_AllPix)	Average VI value over all pixels of the microplot.	✓	✓	✓	✓	✓
	#Frac(GreenPix)	GF given by the fraction of green pixels obtained by thresholding the VI image. The resulting best GF estimate, $GF_{GREENPIX}$, is then transformed into log(1- $GF_{GREENPIX}$) for GAI estimation.	✓	✓	-	-	-
	#Avg(VI_GreenPix)	Average VI value over a fraction of green pixels (all, only darkest, or only brightest green pixels).	-	-	✓	-	-
	#GAI.C_{ab}	Product of best GAI and C_{ab} estimates.	-	-	-	✓	✓
	#MLR	Multiple Linear Regression using log(1-$GF_{GREENPIX}$) (or $GF_{GREENPIX}$ for GF estimation) and VI_{CAB} as inputs.	✓	✓	-	✓	✓

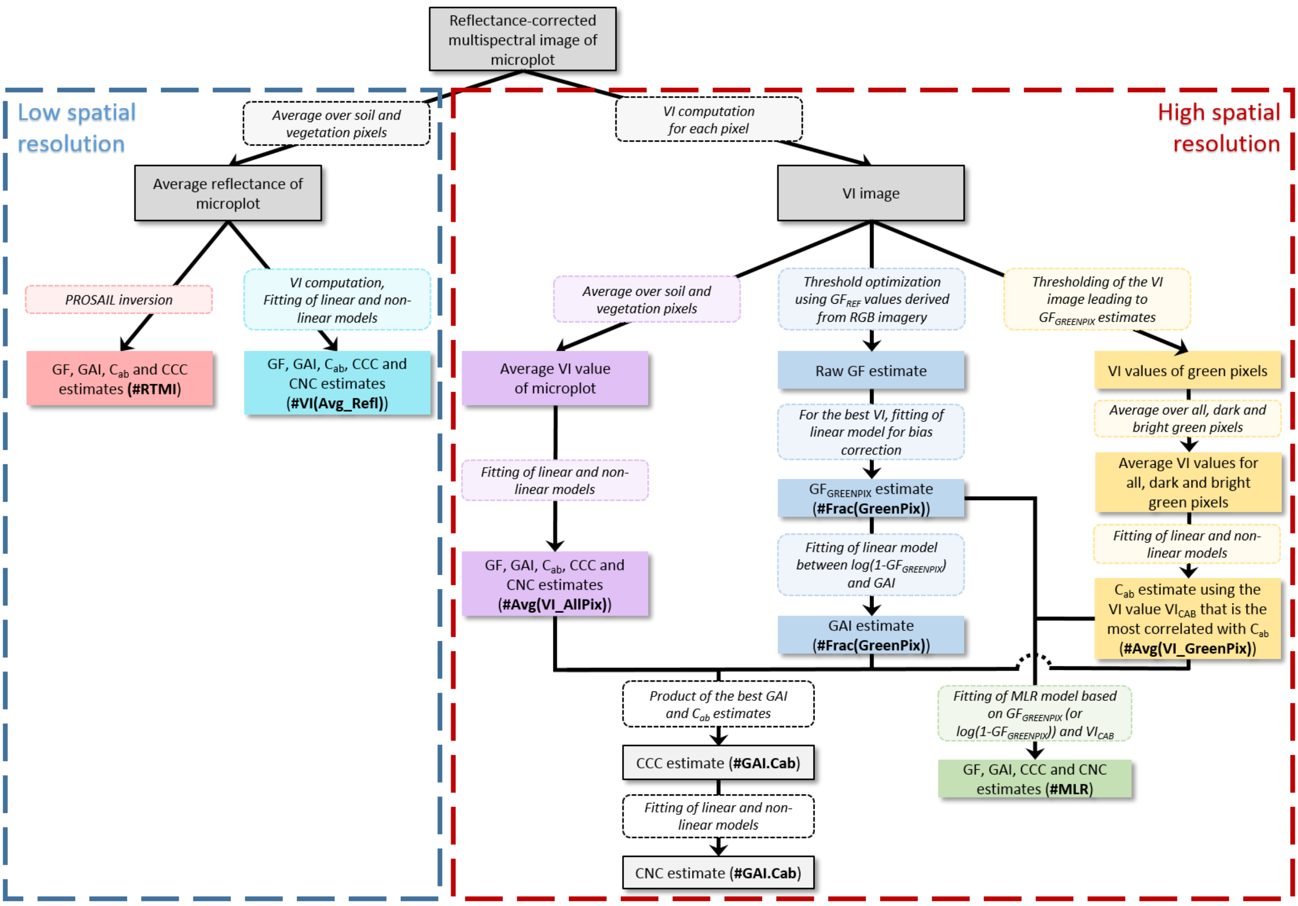

Fig. 3: Flowchart illustrating the seven methods used to estimate GF, GAI, C_{ab}, CCC and CNC from UAV multispectral images of microplots. The blue (resp., red) panel on the left-hand (resp., right-hand) side corresponds to methods to be used with low (resp., high) spatial resolution data.

2.5.1. Selection of VIs

A number of VIs were selected from the literature based on their sensitivity to GF, GAI, C_{ab}, CCC and CNC (Table 3). All of them were expressed as ratios of two or three wavebands. Such VIs indeed minimized the influence of multiplicative factors, including possible variation in the illumination conditions during the flights. An extensive discussion of the properties of the selected VIs can be found in Jay et al. (2017a). In this study, the Visible Atmospherically Resistant Index ($VARI$) was also included in the comparison, as it was demonstrated to be strongly related to GF (Gitelson et al., 2002).

All the six VIs selected were originally designed using wavebands that may not be available on the band set chosen for the AIRPHEN multispectral camera. Therefore, each band in the original formulation of each VI was replaced by the closest band available (Table 3). Note that the 560 nm band used in 2016 and the 570 nm band used in 2017 were not considered to prevent potential artifacts between years.

Table 3 : Ratio VIs selected from the literature.

VI name	References	VI formulation used in this study
$VARI$	Gitelson et al. (2002)	$\frac{R_{530} - R_{675}}{R_{530} + R_{675} - R_{450}}$
$NDVI$	Rouse et al. (1973)	$\frac{R_{850} - R_{675}}{R_{850} + R_{675}}$
CI_{green}	Gitelson et al. (2006a, 2005, 2003)	$\frac{R_{850}}{R_{530}} - 1$
CI_{re}	Gitelson et al. (2006a, 2005, 2003)	$\frac{R_{850}}{R_{730}} - 1$
$MTCI$	Dash and Curran (2004)	$\frac{R_{850} - R_{730}}{R_{730} - R_{675}}$
mND_{blue}	Jay et al. (2017a)	$\frac{R_{450} - R_{730}}{R_{450} + R_{850}}$

2.5.2. Estimation approaches exploiting the centimeter resolution of UAV multispectral imagery

- *#Avg(VI_AllPix): using the average VI value over all the pixels of the microplot*. Here, the VI value was the average of the VI values computed for all the soil and vegetation pixels of the UAV image of the microplot (Fig. 3). This average was computed using a 1 % trimmed mean to remove possible outliers present in the tails of the VI distributions. Four linear and non-linear (second-degree polynomial, power and exponential functions) prediction models were then built using all the UAV multispectral images available for each targeted variable.
- *#Frac(GreenPix): estimating GF and GAI using a fraction of green pixels derived from VI thresholding*. For each microplot, green pixels were identified by thresholding the six VI images. For each VI, the threshold value was optimized to get the best match between the reference GF value GF_{REF} derived from the RGB image classification (section 2.4.1), and the GF value given by the fraction of green pixels after VI image thresholding (Fig. 3). Furthermore, the raw estimated GF value obtained by thresholding the VI image could be linearly related to GF_{REF} to remove possible bias. This corrected GF

estimate is called $GF_{GREENPIX}$, and is also used in the following #MLR approach. In the case of GAI estimation, $GF_{GREENPIX}$ was transformed into log(1-$GF_{GREENPIX}$) and linearly related to GAI according to Nilson (1971) and Weiss et al. (2004).

- *#Avg(VI_GreenPix): estimating C_{ab} using the average VI value computed over a fraction of green pixels.* Similarly to Jay et al. (2017a), VIs were here computed based on three subsets of green pixels extracted using the available centimeter-scale UAV multispectral imagery, i.e., (i) all the green pixels, (ii) the 50 % darkest green pixels or (iii) the 50 % brightest green pixels. The green pixels were first identified using the optimal threshold leading to the $GF_{GREENPIX}$ estimates obtained with the previous #Frac(GreenPix) approach (Fig. 3). However, the threshold value leading to optimal C_{ab} estimation may differ from the value leading to optimal GF estimation due to the detrimental influence of mixed pixels containing both soil and vegetation. Therefore, the performance of C_{ab} estimation was also investigated for other selections of green pixels obtained for several threshold values around the optimal value leading to $GF_{GREENPIX}$ estimates. Then, for each selected fraction of green pixels, the 50 % darkest and 50 % brightest pixels were identified based on the value in the near-infrared (NIR) band. For each subset of pixels considered, the average VI values were computed using a 1 % trimmed mean as for #Avg(VI_Refl), and linearly and non-linearly related to C_{ab}. Note that this approach focusing on green pixels was only used for C_{ab} estimation. The VI computed over the selected fraction of green pixels that provides the best C_{ab} estimation performance is called VI_{CAB} when used in the following #MLR approach.
- *#GAI.C_{ab}: estimating CCC and CNC using the product of the best GAI and C_{ab} estimates*. CCC could be estimated either directly as in approach #Avg(VI_AllPix), or as the product of the best GAI and C_{ab} estimates (Fig. 3). Since leaf nitrogen content shows some correlation with leaf chlorophyll content (Jay et al., 2017b; Schlemmer et al., 2013), CNC was also linearly and non-linearly related to this product (Fig. 3).
- *#MLR: estimating GF, GAI, CCC and CNC using Multiple Linear Regression*. In the #MLR approach, a Multiple Linear Regression (MLR) model was built, combining (i) $GF_{GREENPIX}$ or log(1- $GF_{GREENPIX}$) derived

from approach #Frac(GreenPix) and carrying information on canopy structure, and (ii) VI_{CAB} derived from approach #Avg(VI_GreenPix) and carrying information on leaf chlorophyll content (Fig. 3). These two input variables were assumed to bring complementary information on the targeted plant traits. These input variables were first standardized according to:

$$X_i = \frac{(x_i - \overline{x_i})}{\sigma_{x_i}} \quad (2)$$

where $\overline{x_i}$ and σ_{x_i} are, respectively, the average and standard deviation values of input variable x_i in the calibration set, with $[x_1, x_2]$ = [$GF_{GREENPIX}$, VI_{CAB}]. Note that, in the case of GAI, CCC and CNC estimation, we took $x_1 = \log(1 - GF_{GREENPIX})$. A MLR model was then built according to:

$$Y = \alpha_0 + \sum_{i=1}^{2} \alpha_i X_i \quad (3)$$

where Y is the variable to be estimated, and α_i the MLR coefficients to be calibrated.

2.5.3. Standard remote-sensing approaches using the average reflectance of the microplot

- *#RTMI: inverting the PROSAIL model.* The #RTMI (standing for Radiative Transfer Model Inversion, Table 2 and Fig. 3) approach consists in inverting the PROSAIL radiative transfer model (Baret et al., 1992; Jacquemoud et al., 2009), combining the PROSPECT model (Jacquemoud and Baret, 1990) with the SAIL model (Verhoef, 1985, 1984). PROSAIL simulates the canopy bidirectional reflectance of a turbid medium canopy as a function of leaf biochemical and canopy structural variables for a given sun-sensor geometry. Although PROSAIL may not be fully optimal for modeling the reflectance of row-structured sugar beet canopies, a number of studies have demonstrated that it enables accurate retrievals of GAI, C_{ab} and CCC for such vegetation arrangements (Dorigo, 2012; Duan et al., 2014; Jacquemoud et al., 1995; Jay et al., 2017b; Verger et al., 2014).

The PROSPECT 3 model (Baret and Fourty, 1997) was used in this study, as Jiang et al. (2018) showed that this PROSPECT version generally shows similar performance as the latest versions (Feret et al., 2008; Féret et al., 2017) while having less variables to be inverted. It simulates the leaf directionalhemispherical reflectance and transmittance as a function of a structure parameter (N, unitless) as well as leaf chlorophyll (C_{ab}, in µg/cm²), dry matter (C_m, in g/cm²), water (C_w, in g/cm²) and brown pigment (C_{bp}, unitless) contents. SAIL accounts for the effects of leaf reflectance and transmittance, green area index (GAI, unitless), average leaf angle (ALA, in °), soil brightness factor (B_s, unitless), viewing zenith angle (θ_v, in °), solar zenith angle (θ_s, in °) and relative azimuth angle (ϕ_{sv}, in °). A parameter (s_L, unitless) was also included to account for the hotspot effect (Kuusk, 1991; Verhoef, 1998).

In this paper, each UAV-measured canopy reflectance obtained by averaging all the vegetation and soil pixels of each microplot was inverted using a PROSAIL inversion approach based on artificial neural network. Following Verger et al. (2014), the inputs of the neural network were the solar zenith and azimuth angles, the viewing zenith angle, and the first five bands normalized by the 850 nm band so as to better handle possible variation in the illumination conditions. More details on the neural network architecture and training data base can be found in Weiss et al. (2002), Verger et al. (2011) and Li et al. (2015). Note that GF and CCC can be directly estimated using this inversion method. In the case of CCC, the obtained estimate may differ from the product of GAI and C_{ab} estimated values. Note also that it is not possible to estimate directly CNC since leaf nitrogen content is not explicitly accounted for by the leaf PROSPECT model.

- *#VI(Avg_Refl): using the VI value computed from the average microplot reflectance.* The six VIs were computed from the canopy reflectance obtained by averaging over all the vegetation and soil pixels of the UAV image of the microplot (Fig. 3). The VIs were then linearly and non-linearly related to each targeted variable, similarly as #Avg(VI_AllPix) (section 2.5.2). Note that approach #VI(Avg_Refl) does not exploit the centimeter resolution of UAV multispectral images, unlike the previous #Avg(VI_AllPix) approach for which each VI was computed by averaging pixel-level VI values. As the six VIs tested are non-linear functions of reflectance, these two approaches may obtain different results (Jay et al., 2017a; Steven et al., 2015).

2.5.4. Performance assessment

A cross-validation process was used to quantify the performances of the six VI-based approaches (Table 2). It consisted in calibrating a prediction model using N-1 dates out of the N available (Table 1) and using the last date for the validation. This process was repeated N times to use every date available for the validation. Note that in the case of approach #MLR, each of the N calibration and validation sets was standardized using the $\overline{x_i}$ and σ_{x_i} values computed over the corresponding calibration set (Eq. (2)). Four indicators of the prediction performance were then computed, namely, the root mean square error of prediction (RMSEP), the relative RMSEP (RRMSEP) being defined as the ratio of the RMSEP to the mean measured value, the squared Pearson's correlation coefficient (r^2) between estimated and measured values, and the coefficient of determination defined as $R^2 = 1 - \frac{RMSEP^2}{\sigma_{tot}^2}$, where σ_{tot}^2 is the total variance of the measured variable.

3. Results

3.1. Ground-based measurements

Table 4 : Statistics of GF, GAI, C_{ab}, CCC and CNC measurements.

Variable	Unit	Number of microplots	Min - Max	Mean	Standard deviation	Coefficient of variation (%)
GF	-	238	0.18 - 0.97	0.61	0.25	40
GAI	-	135	0.13 - 4.57	1.50	1.00	67
C_{ab}	µg/cm²	177	21.2 - 51.1	33.7	7.0	21
CCC	g/m²	92	0.04 - 1.46	0.52	0.39	74
CNC	g/m²	114	0.7 - 16.8	6.4	3.9	61

A large variability is observed for each structural and biochemical variable of interest (Table 4). Importantly, C_{ab} and canopy structure variables (GAI and GF) poorly correlate (Table 5), which ensures that any correlation between VIs and C_{ab} will not derive from the covariance with either GF or GAI. Conversely, strong correlations are observed between GF and GAI (Table 5), as already outlined by Andrieu et al. (1997) for sugar beet crops. Note that, as expected, the linear correlation between GF and GAI slightly increases when transforming GF into log(1-GF) to better account for the saturation observed for high GAI values (Andrieu et al., 1997; Nilson, 1971; Weiss et al., 2004). GAI strongly correlates with CCC (Table 5) because of the larger variability in GAI as compared to that in C_{ab} (Table 4). Table 5 also shows strong correlations between CNC and GAI, as well as between CNC and CCC. However, these correlations should be taken with caution due to the low number of samples considered (24) and to the poorer correlations between CNC and log(1-GF) obtained with a larger number of samples (96).

Table 5 : Squared Spearman's (ρ^2, lower diagonal) and Pearson's (r^2, upper diagonal) correlation coefficients between the five variables targeted. The variable log(1-GF) is also included to show the gain in linear correlation obtained with this transformation. For each pair of variables, the number of microplots available to compute the correlation is indicated in parentheses. Colors show the level of correlation, ranging from pale yellow for low correlation to red for high correlation.

ρ^2 \ r^2	GF	log(1-GF)	GAI	C_{ab}	CCC	CNC
GF	-	0.87 (238)	0.81 (*117*)	0.11 (*159*)	0.79 (*86*)	0.58 (*96*)
log(1-GF)	1.00 (238)	-	0.83 (*117*)	0.03 (*159*)	0.81 (*86*)	0.50 (*96*)
GAI	0.89 (*117*)	0.89 (*117*)	-	0.07 (*87*)	0.91 (*92*)	0.82 (*24*)
C_{ab}	0.07 (*159*)	0.07 (*159*)	0.11 (*87*)	-	0.21 (*87*)	0.10 (*113*)
CCC	0.86 (*86*)	0.86 (*86*)	0.95 (*92*)	0.24 (*87*)	-	0.84 (*24*)
CNC	0.62 (*96*)	0.62 (*96*)	0.83 (*24*)	0.04 (*113*)	0.87 (*24*)	-

3.2. Correlations between VIs

The correlations between VIs computed over soil and vegetation pixels shows that $VARI$ and $NDVI$ are strongly related, with squared Spearman's correlation coefficients (ρ^2) higher than 0.93 (Table 6). These two VIs show high to intermediate correlations with CI_{green} and CI_{re} ($0.49 \leq \rho^2 \leq 0.83$), both of which are themselves strongly related ($\rho^2 = 0.87$). On the other hand, mND_{blue} and $MTCI$ generally poorly correlate with other VIs ($\rho^2 \leq 0.53$). Note that the Spearman's and Pearson's correlation coefficients are generally similar, indicating that the relationships are approximately linear.

Table 6 : Squared Spearman's (ρ^2, lower diagonal) and Pearson's (r^2, upper diagonal) correlation coefficients between VIs computed over all soil and vegetation pixels and over all the 274 microplots. For each microplot, each VI is computed

from the average of pixel-level VI values. Colors show the level of correlation, ranging from pale yellow for low correlation to red for high correlation.

ρ^2 \ r^2	$VARI$	$NDVI$	CI_{green}	CI_{re}	$MTCI$	mND_{blue}
$VARI$	-	0.94	0.65	0.49	0.01	0.55
$NDVI$	0.93	-	0.80	0.63	0.06	0.53
CI_{green}	0.64	0.83	-	0.90	0.32	0.18
CI_{re}	0.49	0.66	0.87	-	0.56	0.04
$MTCI$	0.00	0.03	0.19	0.40	-	0.15
mND_{blue}	0.53	0.42	0.21	0.07	0.17	-

$VARI$ and $NDVI$ still strongly correlate ($\rho^2 = 0.80$) when computed over vegetation pixels (Table 7). However, in this case, only $NDVI$ shows significant correlations with the other VIs tested, with maximum ρ^2 values of 0.73 and 0.49 with CI_{green} and CI_{re}, respectively. $MTCI$, CI_{re}, CI_{green} and, to a lesser extent, mND_{blue}, strongly correlate with each other, with a maximum correlation between $MTCI$ and CI_{re} ($\rho^2 = 0.97$), and a minimum correlation between CI_{green} and mND_{blue} ($\rho^2 = 0.20$). Here again, the similar Spearman's and Pearson's correlation coefficients indicate that the relationships are approximately linear.

Table 7 : Squared Spearman's (ρ^2, lower diagonal) and Pearson's (r^2, upper diagonal) correlation coefficients between VIs computed over all green pixels and over all the 274 microplots. For each microplot, each VI is computed from the average of pixel-level VI values. Colors show the level of correlation, ranging from pale yellow for low correlation to red for high correlation.

ρ^2 \ r^2	$VARI$	$NDVI$	CI_{green}	CI_{re}	$MTCI$	mND_{blue}
$VARI$	-	0.79	0.30	0.19	0.13	0.00
$NDVI$	0.80	-	0.69	0.52	0.43	0.07
CI_{green}	0.33	0.73	-	0.87	0.81	0.38
CI_{re}	0.21	0.49	0.81	-	0.99	0.70
$MTCI$	0.12	0.36	0.72	0.97	-	0.77
mND_{blue}	0.01	0.02	0.20	0.51	0.63	-

3.3. Estimation of canopy structure

3.3.1. GF estimation

Since GF may play a particular role in the estimation of the other variables when exploiting the centimeter resolution of UAV images, emphasis is first put on it.

When using the average microplot reflectance, the GF values estimated using PROSAIL inversion (approach #RTMI) strongly correlate with the measured ones ($r^2 = 0.91$) (Fig. 4.a). However, the results are penalized by a significant underestimation for the largest GF values, resulting in $RMSEP = 0.15$ ($RRMSEP = 25\%$). The bias is removed when using #VI(Avg_Refl) based on VIs computed over average microplot reflectances (Fig. 4.b). Significantly better predictions are obtained using $VARI$ and a second-degree polynomial, with $RMSEP = 0.05$ ($RRMSEP = 8$ %, Table 8, Fig. 4.b).

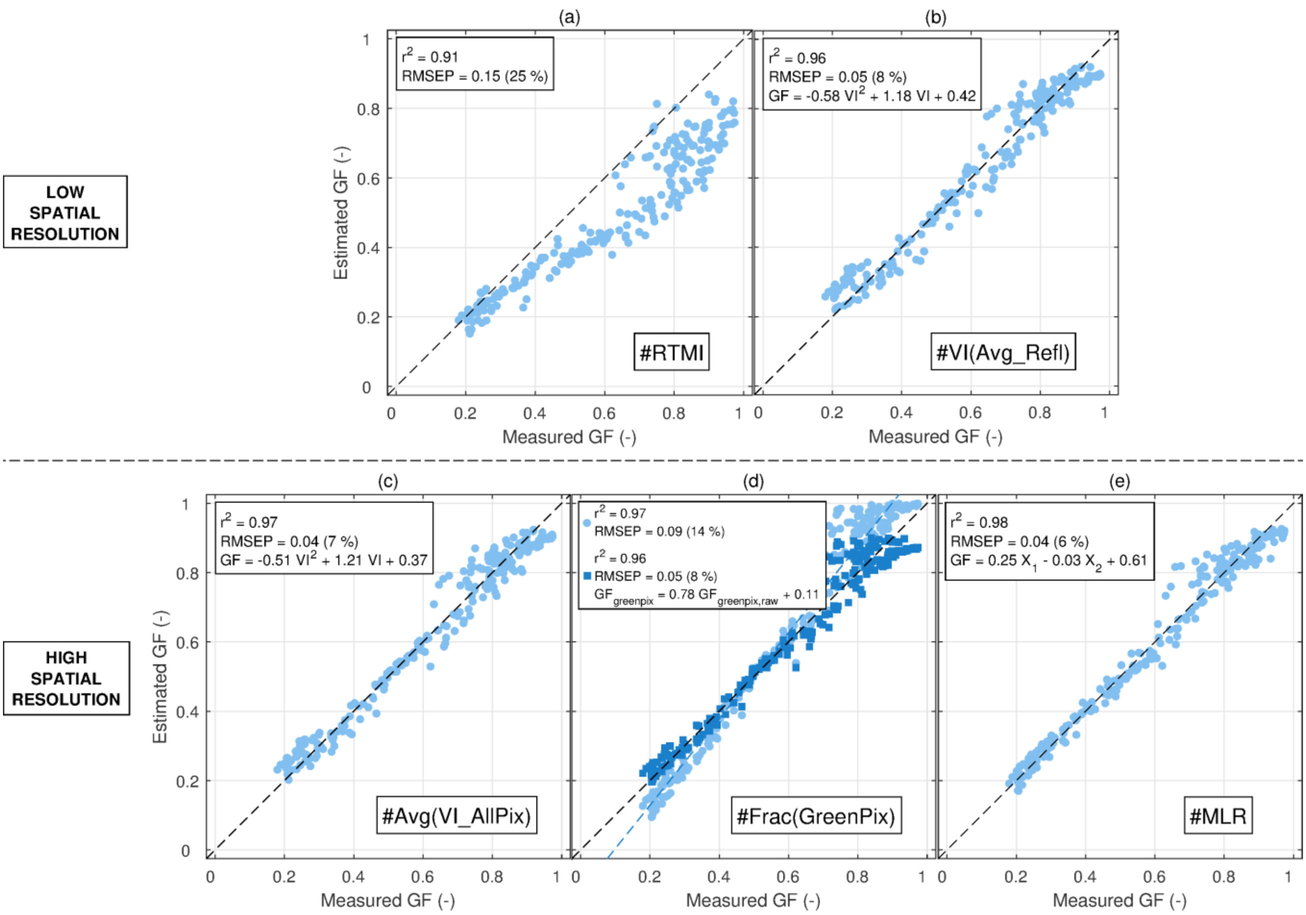

Fig. 4 : GF estimation results obtained using low and high spatial resolution approaches: (a) #RTMI based on PROSAIL inversion, (b) #VI(Avg_Refl) with $VARI$ and a second-degree polynomial, (c) #Avg(VI_AllPix) with $VARI$ and a second-degree polynomial, (d) #Frac(GreenPix) with $VARI$ and a threshold of 0.14 before (disks in light blue) and after (squares in dark blue) correcting for the bias affecting the raw GF estimate $GF_{GREENPIX,RAW}$, and (e) #MLR based on standardized $GF_{GREENPIX}$ (Fig. 4.d) and VI_{CAB} (Fig. 6.d) values. For each method, the squared Pearson's correlation coefficient (r^2) and the RMSEPs in absolute and relative (in %) are indicated. The regression equation is also shown for empirical approaches.

Table 8 : RMSEPs obtained for the estimation of GF (unitless), GAI (unitless), C_{ab} (in µg/cm²), CCC (in g/m²) and CNC (in g/m²) using VIs computed either from the average microplot reflectance (#VI(Avg_Refl)) or from the average of pixel-level VI values over all microplot pixels (#Avg(VI_AllPix)). For each method, each variable and each VI, only the RMSEP

obtained with the best model is shown (results obtained with the four linear and non-linear models tested are provided in supplementary material). For each column, the best result is in bold.

VI	#VI(Avg_Refl)					#Avg(VI_AllPix)				
	GF	GAI	C_{ab}	CCC	CNC	GF	GAI	C_{ab}	CCC	CNC
$VARI$	**0.05**	**0.42**	7.4	**0.19**	2.7	**0.04**	**0.40**	7.7	**0.19**	2.7
$NDVI$	0.07	0.46	7.6	0.20	2.2	0.07	0.44	7.6	0.19	2.2
CI_{green}	0.18	0.69	6.9	0.24	**2.1**	0.18	0.70	6.9	0.24	**2.1**
CI_{re}	0.21	0.74	5.4	0.20	3.2	0.20	0.74	5.2	0.20	3.1
$MTCI$	0.25	0.93	**4.2**	0.25	3.6	0.29	1.10	**4.2**	0.32	4.8
mND_{blue}	0.21	0.87	7.7	0.41	5.3	0.19	0.82	7.4	0.40	5.1

When exploiting the centimeter resolution of UAV images through approach #Avg(VI_AllPix) for which each VI value is the average of the VI image, a slight improvement is observed when using $VARI$ ($RMSEP = 0.04$, Fig. 4.c), followed by $NDVI$ ($RMSEP = 0.07$) (Table 8). When using approach #Frac(GreenPix), GF is given by the fraction of green pixels computed by thresholding the VI image. The optimal threshold used here is determined using the reference GF derived from RGB image classification. The best GF estimation results are obtained using $VARI$ images and an optimal threshold of $VARI = 0.14$ ($RMSEP = 0.09$, Table 9), followed by $NDVI$ images and an optimal threshold of $NDVI = 0.62$ ($RMSEP = 0.11$, Table 9). It is worth noting that similarly accurate results are obtained for a range of $VARI$ values around the optimal value of 0.14, e.g., the $RMSEP$ remains lower than 0.11 when taking a $VARI$ threshold between 0 and 0.25 (see the figure in supplementary material). However, these results show some underestimation for low GF values and some overestimation for large GF values (Fig. 4.d). A linear regression was thus applied to correct for this bias, leading to improved performance with $RMSEP = 0.05$ (Table 9, Fig. 4.d). The resulting GF estimates are called $GF_{GREENPIX}$ and used as complementary information to improve the estimation of canopy variables through the #MLR approach. Further, green pixels selected by thresholding the $VARI$ images will be used in the following sections.

Here, approach #MLR consists in combining the two input variables [$GF_{GREENPIX}$, VI_{CAB}], where VI_{CAB} is the mND_{blue} value averaged over the 50 % darkest green pixels (the green pixels being defined by $VARI > 0.20$, see section 3.4.1). Using VI_{CAB} as additional explanatory variable within #MLR slightly improves the GF estimation results obtained with #Frac(GreenPix), with $RMSEP = 0.04$ ($RRMSEP = 6\%$) (Fig. 4.e).

Table 9 : Results obtained for the estimation of GF using the #Frac(GreenPix) approach, consisting in retrieving the fraction of green pixels by thresholding the VI images. For each VI, the RMSEP (unitless) before and after bias correction is shown, and the best result is in bold.

VI	Optimal threshold value	RMSEP before bias correction (-)	RMSEP after bias correction (-)
$VARI$	0.14	**0.09**	**0.05**
$NDVI$	0.62	0.11	0.06
CI_{green}	2.20	0.16	0.12
CI_{re}	0.15	0.16	0.16
$MTCI$	0.22	0.23	0.24
mND_{blue}	-0.68	0.37	0.30

3.3.2. GAI estimation

The GAI estimation results obtained when using the average microplot reflectance show similar characteristics as the GF estimation results. In the case of approach #RTMI, the measured and estimated GAI values strongly correlate ($r^2 = 0.85$); however, #RTMI significantly underestimates GAI for the largest values, leading to $RMSEP = 0.53$ ($RRMSEP = 35\%$) (Fig. 5.a). The retrieval accuracy improves when using #VI(Avg_Refl), with the same hierarchy between VIs being observed for GF and GAI (Table 8). The best predictions are obtained with $VARI$ and a linear model ($RMSEP = 0.42$) (Fig. 5.b). Note, however, that GAI is still underestimated for $GAI \geq 3.00$ (Fig. 5.b).

Similarly to GF, exploiting the image centimeter resolution through approach #Avg(VI_AllPix) slightly improves the best performance obtained with approach #VI(Avg_Refl) based on the average microplot reflectance (Table 8). The best predictions are obtained using $VARI$ ($RMSEP = 0.40$ with a linear model, Fig. 5.c), followed by $NDVI$ ($RMSEP = 0.44$ with an exponential model, Table 8). Approach #Frac(GreenPix) for which GAI is linearly related to log(1- $GF_{GREENPIX}$) further improves GAI estimation, with $RMSEP = 0.38$ (Fig. 5.d). Finally, similar GAI estimates ($RMSEP = 0.39$, Fig. 5.e) are obtained when using approach #MLR based on the two input variables [log(1- $GF_{GREENPIX}$), VI_{CAB}], where VI_{CAB} is the mND_{blue} value averaged over the 50 % darkest green pixels (the green pixels being defined by $VARI > 0.20$, see section 3.4.1). Note that the three methods exploiting the centimeter resolution still show some underestimation for $GAI \geq 3.00$, similarly to approaches based on average microplot reflectance (Fig. 5).

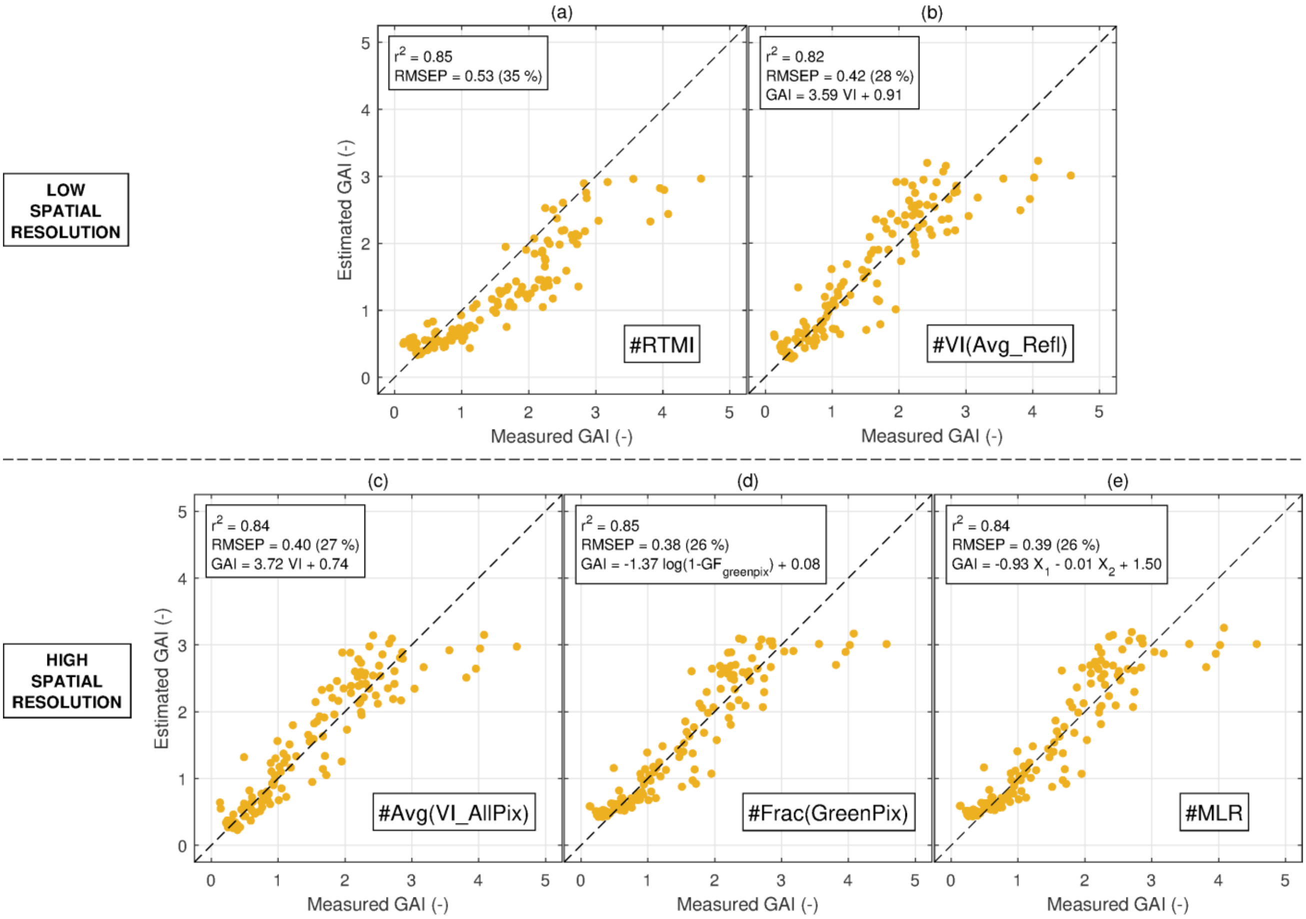

Fig. 5 : GAI estimation results obtained using low and high spatial resolution approaches: (a) #RTMI based on PROSAIL inversion, (b) #VI(Avg_Refl) with $VARI$ and a linear model, (c) #Avg(VI_AllPix) with $VARI$ and a linear model, (d) #Frac(GreenPix) with log(1-$GF_{GREENPIX}$) and a linear model, and (e) #MLR based on standardized log(1-$GF_{GREENPIX}$) (Fig. 4.d) and VI_{CAB} (Fig. 6.d) values. For each method, the squared Pearson's correlation coefficient (r^2) and the RMSEPs in absolute and relative (in %) are indicated. The regression equation is also shown for empirical approaches.

3.4. Estimation of canopy biochemistry

3.4.1. C_{ab} estimation

For C_{ab} estimation, inverting PROSAIL based on the average microplot reflectance results in relatively poor performance ($RMSEP$ = 5.9 µg/cm², Fig. 6.a). Note that the dispersion around the 1:1 line is greater for samples with C_{ab} values around 30 µg/cm² (Fig. 6.a). Further investigation shows that, although having similar C_{ab} values, these samples are characterized by strongly different canopy structures, with GF ranging from 0.20 to 0.97 and a standard deviation of 0.28. Using VIs through approach #VI(Avg_Refl) significantly improves C_{ab}

estimation, with $MTCI$ and, to a lesser extent, CI_{re}, performing better than the other VIs tested (Table 8). The best predictions are obtained using $MTCI$ and a second-degree polynomial ($RMSEP = 4.2$ µg/cm², Fig. 6.b).

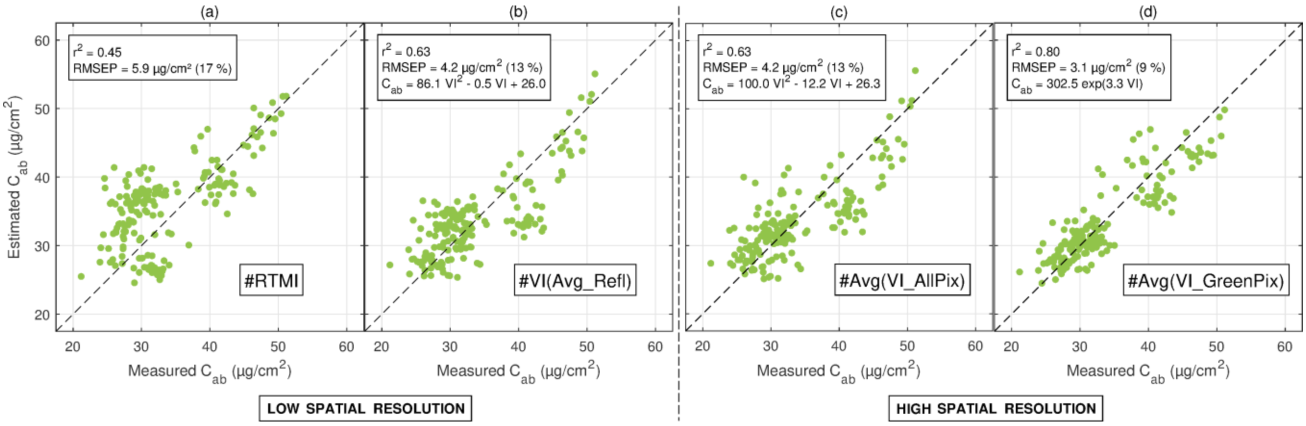

Fig. 6 : C_{ab} estimation results obtained using low and high spatial resolution approaches: (a) #RTMI based on PROSAIL inversion, (b) #VI(Avg_Refl) with $MTCI$ and a second-degree polynomial, (c) #Avg(VI_AllPix) with $MTCI$ and a second-degree polynomial, and (d) #Avg(VI_GreenPix) with a $VARI$ threshold of 0.20, and an exponential model relating C_{ab} and mND_{blue} values averaged over the darkest green pixels. For each method, the squared Pearson's correlation coefficient (r^2) and the RMSEPs in absolute and relative (in %) are indicated. The regression equation is also shown for empirical approaches.

Approach #Avg(VI_AllPix) based on the average VI value of the microplot (Fig. 6.c) shows nearly the same performances as approach #VI(Avg_Refl) based on the average microplot reflectance (Table 8). A similar hierarchy between VIs is observed, with $MTCI$ leading to the best performance ($RMSEP = 4.2$ µg/cm²), and $VARI$, $NDVI$ and mND_{blue} to the worst ones ($RMSEP \geq 7.4$ µg/cm²).

Focusing on any of the three selections of green pixels identified using the $VARI$ image (using the threshold $VARI = 0.14$) and the near-infrared band (section 2.5.2), makes the measured optical signature get closer to a typical leaf signature, e.g., with a sharper increase in reflectance observed in the red-edge region (Fig. 7).

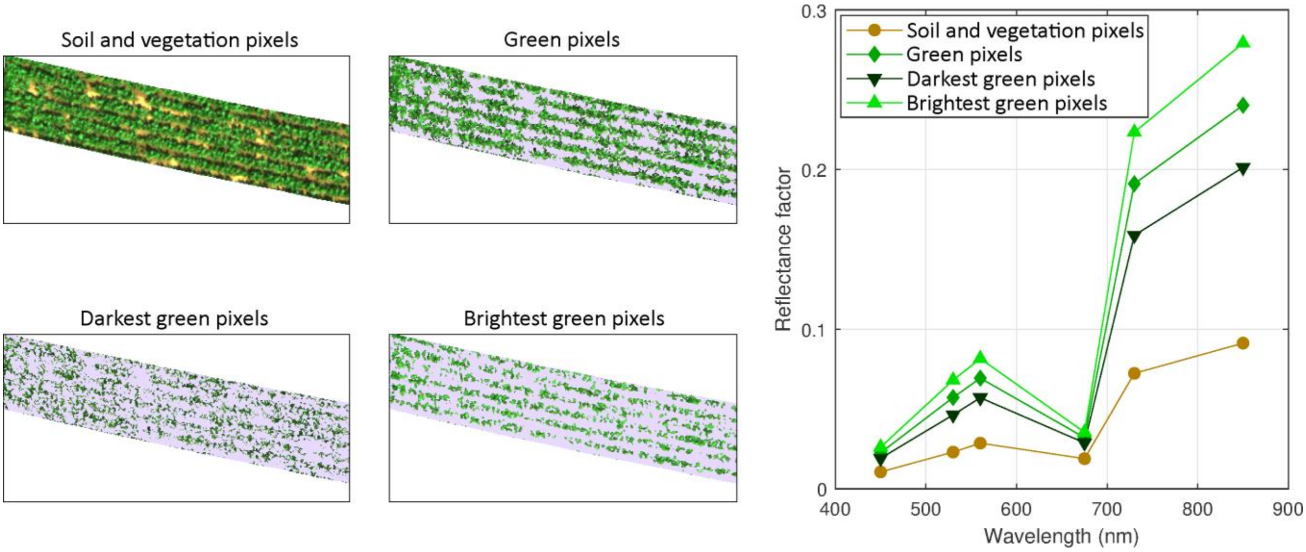

Fig. 7 : Subsets of pixels extracted from a multispectral image of a single microplot, and corresponding average reflectance spectra. Pixels are here discriminated using a $VARI$ threshold of 0.14 (section 3.3.1). Purple areas show the pixels excluded from the spectral average for each subset.

Consequently, approach #Avg(VI_GreenPix) generally improves the C_{ab} estimation results obtained with approach #Avg(VI_AllPix) (Fig. 8). For example, the results obtained with $MTCI$ slightly improves when focusing on the 50 % darkest green pixels ($RMSEP = 3.9$ µg/cm²). However, in the case of mND_{blue}, this improvement is much more significant, with $RMSEP = 3.2$ µg/cm² obtained when considering the 50 % darkest green pixels (Fig. 8). Note that $VARI$, $NDVI$ and CI_{green} provide significantly poorer performances than CI_{re}, $MTCI$ and mND_{blue}, and show no to little improvement when focusing on either selection of green pixels (Fig. 8).

The threshold value $VARI = 0.14$ leading to optimal green segmentation (section 3.3.1) also appears to be appropriate for C_{ab} estimation (Fig. 8). Varying the threshold value around 0.14 shows little impact on the performances for the six VIs, especially for $VARI$ values between 0.05 and 0.35. The best C_{ab} estimation results are obtained using a threshold value $VARI = 0.20$, mND_{blue} computed over the darkest green pixels, and an exponential model ($RMSEP = 3.1$ µg/cm², Fig. 6.d). Note that using a linear model leads to similar performance ($RMSEP = 3.3$ µg/cm², not shown). For each microplot, the VI_{CAB} input variable used within the #MLR approach thus corresponds to the mND_{blue} value averaged over the 50 % darkest green pixels (the green pixels being defined by $VARI > 0.20$).

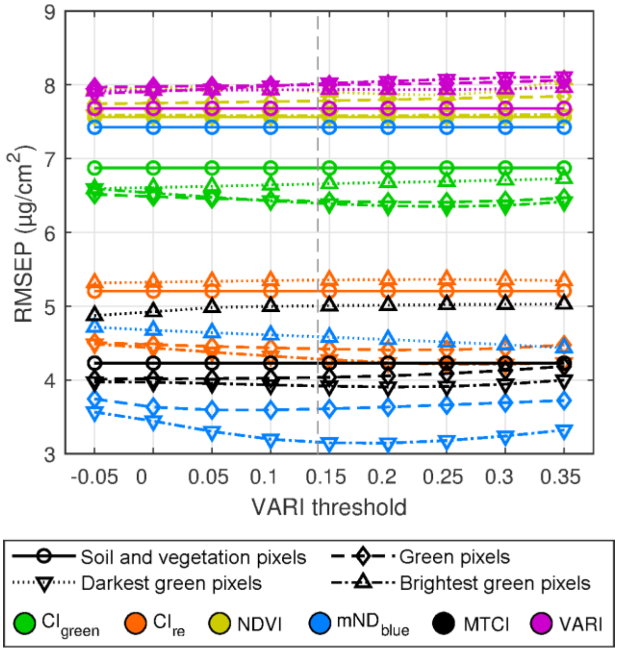

Fig. 8 : RMSEPs obtained for the estimation of C_{ab} using VIs computed as the average of pixel-level VI values over all microplot pixels (#Avg(VI_AllPix)), or over one of the three subsets of green pixels (#Avg(VI_GreenPix)) identified using various $VARI$ thresholds. The vertical dashed line shows the optimal $VARI$ threshold of 0.14 leading to $GF_{GREENPIX}$ (Table 9). For each combination of $VARI$ thresholds, VIs and subsets of pixels, only the RMSEP obtained with the best model (linear or non-linear) is shown.

3.4.2. CCC estimation

Despite a similar bias as for GF and GAI, #RTMI based on PROSAIL inversion provides relatively accurate CCC estimates, with $RMSEP = 0.19$ g/m² (Fig. 9.a). When using VIs computed from average microplot reflectances (#VI(Avg_Refl)), all the VIs except mND_{blue} provides rather similar performances, with RMSEP ranging from 0.19 g/m² for $VARI$ to 0.25 g/m² for $MTCI$ (Table 8, Fig. 9.b). Both approaches #RTMI and #VI(Avg_Refl) generally show a strong dispersion for the highest CCC values (Figs. 9.a-b), corresponding to contrasted combinations of GAI and C_{ab}. For example, in the case of #RTMI and $CCC \geq 1.00$ g/m², the most underestimated CCC values correspond to $GAI \geq 3.00$ and $C_{ab} \leq 40$ µg/cm², while the most accurate CCC estimates correspond to $GAI \approx 2.80$ and $C_{ab} \geq 46$ µg/cm².

Exploiting the centimeter resolution by using the average VI value of the microplot (#Avg(VI_AllPix)) shows negligible difference with the previous #VI(Avg_Refl) approach (Table 8), $VARI$ and a linear model still providing the best performance ($RMSEP = 0.19$ g/m², Fig. 9.c). On the other hand, combining the best GAI and C_{ab} estimates within approach #GAI.C_{ab} leads to a significant 37 % gain in estimation accuracy ($RMSEP =$

0.12 g/m^2) as compared to previous approaches that do not differentiate between green and non-green pixels (Fig. .d). Similarly, the #MLR approach combining log(1-$GF_{GREENPIX}$) and VI_{CAB} also achieves very good performance, with $RMSEP = 0.13$ g/m^2 (Fig. .e).

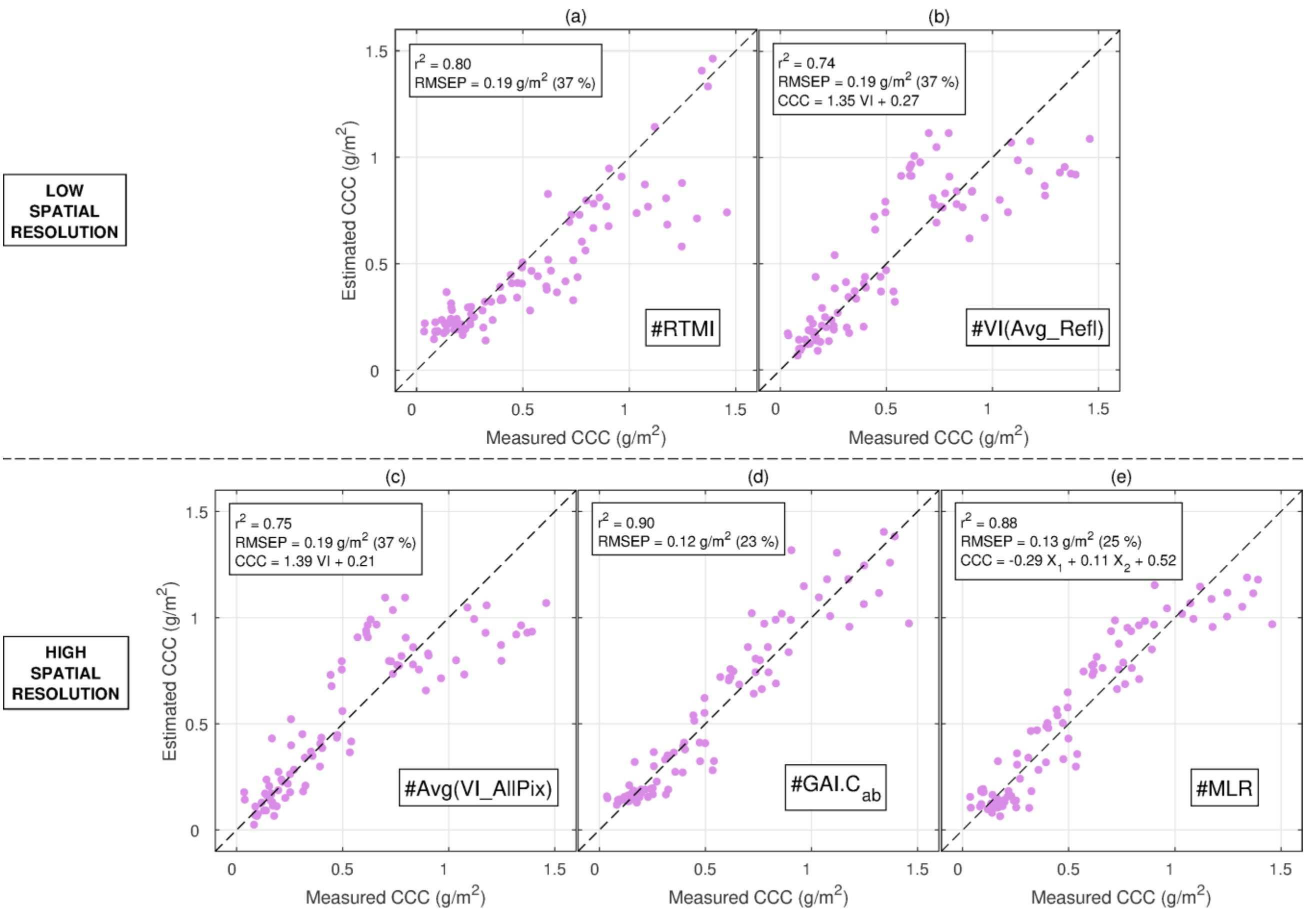

Fig. 9 : CCC estimation results obtained using low and high spatial resolution approaches: (a) #RTMI based on PROSAIL inversion, (b) #VI(Avg_Refl) with $VARI$ and a linear model, (c) #Avg(VI_AllPix) with $VARI$ and a linear model, (d) #GAI.C_{ab}, and (e) #MLR based on standardized log(1-$GF_{GREENPIX}$) (Fig. 4.d) and VI_{CAB} (Fig. 6.d) values. For each method, the squared Pearson's correlation coefficient (r^2) and the RMSEPs in absolute and relative (in %) are indicated. The regression equation is also shown for empirical approaches.

3.4.3. CNC estimation

As outlined in section 2.5.3, approach #RTMI could not be used to estimate CNC, since leaf nitrogen content is not an input variable of the PROSAIL model. When using approach #VI(Avg_Refl) based on average microplot reflectance, CI_{green}, $NDVI$ and $VARI$ provide the most accurate estimates (Table 8). The best results are obtained using CI_{green} and a linear model, with $RMSEP = 2.1$ g/m^2 (Fig. 10.a).

Except for $MTCI$, approach #Avg(VI_AllPix) shows comparable performances as approach #VI(Avg_Refl) (Table 8): CI_{green} still performs the best, with $RMSEP = 2.1$ g/m² and a linear model (Fig. 10.b). Similar results are also obtained using approach #GAI.C$_{ab}$ based on the best GAI and C$_{ab}$ estimates (Fig. 10.c). Further inspection of the results however indicates that #GAI.C$_{ab}$ provides more accurate CNC estimates for $CNC \leq$ 5 g/m². However, for higher CNC values, poor estimates are obtained with the three approaches. Finally, a slight improvement is observed when using approach #MLR, which achieves $RMSEP = 1.9$ g/m² (Fig. 10.d).

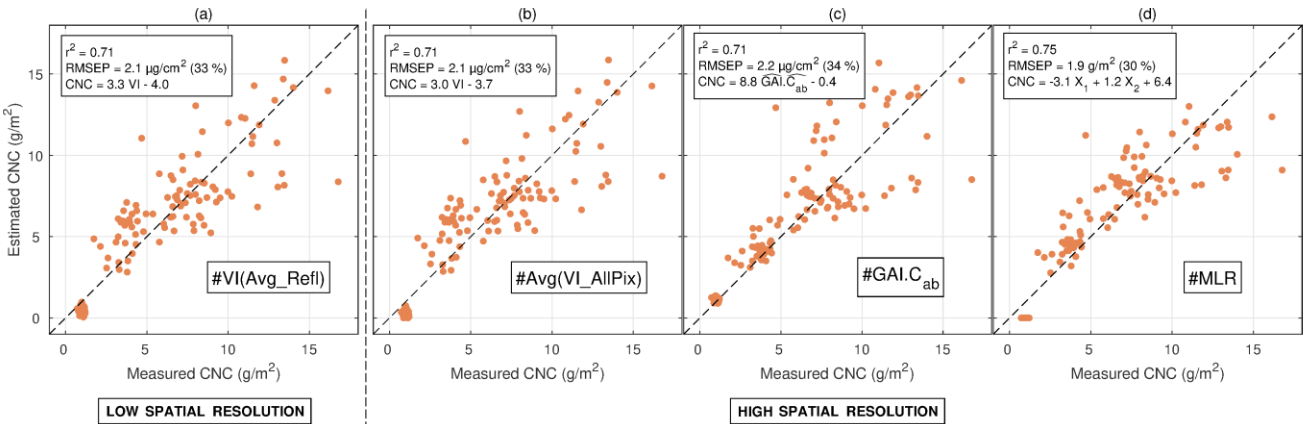

Fig. 10 : CNC estimation results obtained using low and high spatial resolution approaches: (a) #VI(Avg_Refl) with CI_{green} and a linear model, (c) #Avg(VI_AllPix) with CI_{green} and a linear model, (d) #GAI.C$_{ab}$ and a linear model relating CNC and the product of the best GAI and C$_{ab}$ estimates (denoted $\widehat{GAI}$ and $\widehat{C_{ab}}$), and (e) #MLR based on standardized log(1-GF$_{GREENPIX}$) (Fig. 4.d) and VI$_{CAB}$ (Fig. 6.d) values. For each method, the squared Pearson's correlation coefficient (r^2) and the RMSEPs in absolute and relative (in %) are indicated. The regression equation is also shown for empirical approaches.

4. Discussion

All the results presented in sections 3.3 and 3.4 are summarized in Table 10 that will serve as a basis for the following discussion.

Table 10 : Summary of best performances obtained with the seven approaches tested for the estimation of GF, GAI, C_{ab}, CCC and CNC. Performances are here evaluated using the coefficient of determination (R^2). The best VI (when necessary) and best performance are indicated in bold.

Spatial resolution	Approach	GF		GAI		C_{ab}		CCC		CNC	
		VI	R^2	VI	R^2	VI	R^2	VI	R^2	VI	R^2
Low	#RTMI	-	0.63	-	0.72	-	0.30	-	0.75	-	-
	#VI(Avg_Refl)	$VARI$	0.96	$VARI$	0.82	$MTCI$	0.63	$VARI$	0.75	CI_{green}	0.70
High	#Avg(VI_AllPix)	$VARI$	0.97	$VARI$	0.84	$MTCI$	0.64	$VARI$	0.75	CI_{green}	0.70
	#Frac(GreenPix)	$VARI$	0.96	$\boldsymbol{VARI}$	**0.85**	-	-	-	-	-	-
	#Avg(VI_GreenPix)	-	-	-	-	$\boldsymbol{mND_{blue}}$	**0.80**	-	-	-	-
	#GAI.C_{ab}	-	-	-	-	-	-	-	**0.90**	-	0.68
	#MLR	-	**0.98**	-	0.84	-	-	-	0.88	-	**0.75**

4.1. PROSAIL inversion provides less accurate estimates than empirical approaches

When inverting PROSAIL based on average microplot reflectance (approach #RTMI), significant biases are observed for the estimation of GF and GAI (Figs. 4.a and 5.a). Such results are probably due to the turbid medium assumption used to describe the canopy structure within the SAIL model (Verhoef, 1985, 1984). As with ground-based spectro-radiometric measurements (Jay et al., 2017b), this assumption seems to be a limiting factor to accurately characterize the row structure of sugar beet canopies based on UAV observations. Further, the biases observed for GF and GAI affect C_{ab} estimation through a compensation effect well known in optical remote sensing (Baret et al., 2007; Baret and Buis, 2008; Jay et al., 2017b). In particular, the GAI underestimation (Fig. 5.a) is partly compensated for by the C_{ab} overestimation generally observed for samples with similar C_{ab} values around 30 µg/cm² but with strongly different canopy structures (Fig. 6.a). Because of these compensations, the bias observed for the product of GAI and C_{ab}, namely, CCC, is less marked than those observed for GF and GAI. Overall, PROSAIL inversion performs similarly or poorer than empirical approaches for every targeted variable (Table 10). However, when properly exploited, the centimeter-resolution imagery makes it possible to improve the performance for every variable, as we will see in the next sections.

4.2. Exploiting the centimeter resolution to compute VIs leads to more accurate estimates than using VIs computed from average microplot reflectance

Empirical approaches can be applied to VIs computed from average microplot reflectances (#VI(Avg_Refl)), or to VIs averaged over VI images (#Avg(VI_AllPix)) when exploiting the high spatial resolution imagery.

Approaches #VI(Avg_Refl) and #Avg(VI_AllPix) perform similarly (Table 10), although a slight improvement is observed for canopy structure variables (GF, GAI) with #Avg(VI_AllPix). This agrees with the results of Jay et al. (2017a) who suggested that approach #Avg(VI_AllPix) enhances the influence of the heterogeneity due to shadowing and soil effects, which relate to the canopy structure. Another reason is that, unlike #VI(Avg_Refl), approach #Avg(VI_AllPix) used with ratio-based VIs is insensitive to multiplicative variations observed at the pixel level and due mainly to soil brightness (Kauth and Thomas, 1976) and leaf orientation (Jay et al., 2016).

Besides enabling the use of VIs averaged over VI images, the centimeter resolution makes it possible to focus on a subset of pixels of interest. For example, approach #Frac(GreenPix) relates the fraction of green pixels to GF and GAI, while #Avg(VI_GreenPix) uses VI values averaged over the selected darkest green pixels to provide the best C_{ab} estimates (Table 10).

4.3. The $VARI$ index provides the most accurate estimates of canopy structure variables (GF, GAI)

Canopy structure variables (GF and GAI) are best estimated using $VARI$ or $NDVI$ (Tables 8 and 9). The strong correlation between both VIs (Table 6) indicates that they convey similar information for the ranges of GF and GAI values investigated. The remarkable relationship between GF and $VARI$ averaged over all soil and vegetation pixels is consistent with the literature (Gitelson et al., 2002) and makes this VI the most appropriate for accurately retrieving GF in this study. $VARI$ also leads to $GF_{GREENPIX}$, defined as the fraction of green pixels obtained by thresholding the $VARI$ image (approach #Frac(GreenPix)). As GF and GAI are closely but non-linearly related in sugar beet crops (Table 5), GAI can be accurately derived from log(1- $GF_{GREENPIX}$).

Because $VARI$ is based only on visible bands (Table 3) for which leaf and soil reflectances are minimum, it is significantly less affected by multiple scattering caused by surrounding elements as compared to other VIs using a NIR band. Using $VARI$ within approach #Avg(VI_AllPix) thus leads to very accurate and stable GF and GAI estimates, especially when considering a highly heterogeneous data set such as the one used in this study. However, when the canopy reaches nearly full cover for $GAI \geq 3.00$, $VARI$ saturates and becomes insensitive to GAI, especially because it does not use a NIR band that saturates for much higher GAI values (Jacquemoud et al., 2009). This saturation effect and the associated GAI underestimation are clearly visible in Fig. 5 and are consistent with the findings of Andrieu et al. (1997).

Overall, approaches #Avg(VI_AllPix) and #Frac(GreenPix) provide very similar GF and GAI estimation performances (Table 10), especially when considering that GAI reference measurements are also affected by some level of uncertainty (section 2.2). However, approach #Frac(GreenPix) is expected to be more robust than #Avg(VI_AllPix) because it is not based on the whole distribution of $VARI$ values in the image, but only on the number of green pixels whose $VARI$ values exceed 0.14. Therefore, #Frac(GreenPix) is less affected than #Avg(VI_AllPix) by possible non-multiplicative variations in soil reflectance (e.g., between different sites or due to shadows cast by leaves) and illumination conditions (e.g., under variable cloud coverage). The beneficial influence of such robustness properties on the results could have certainly been more visible if the illumination had been more variable during the flights. Yet, these properties are critical in the perspective of applying a unique prediction model over a wide range of soil properties and illumination conditions, e.g., in a phenotyping context.

4.4. The best C_{ab} estimates are obtained using the mND_{blue} index computed over the darkest green pixels

When using average microplot reflectances (#VI(Avg_Refl)), the best performance obtained with $MTCI$ confirms its strong potential for retrieving C_{ab} from meter- to decameter-scale observations (Haboudane et al., 2008; Hunt et al., 2012; Jay et al., 2017b, 2017a). The improved sensitivity to C_{ab} observed when computing the VIs over a selection of green pixels (#Avg(VI_GreenPix)) is mainly due to the reduction of the soil influence, as reported in the literature (Jay et al., 2017a; Moorthy et al., 2008; Zarco-Tejada et al., 2004, 2013, 2001). This gain is very important for mND_{blue} that is extremely sensitive to this detrimental influence (Jay et al., 2017a). Therefore, mND_{blue} performs the best when the $VARI$ threshold used to extract green pixels is sufficiently high to remove most of the soil pixels, including mixed pixels containing both soil and vegetation. In this study, the optimal $VARI$ threshold of 0.14 leading to optimal green segmentation (Table 9) may therefore be slightly increased up to 0.20 to remove more mixed pixels, thus reaching best C_{ab} estimation.

Further, focusing on the dark green pixels rather than on the bright ones appears to be more effective for C_{ab} estimation, which is inconsistent with previous studies (Jay et al., 2017a; Moorthy et al., 2008; Zarco-Tejada et al., 2004, 2013, 2001). Leaf surface contribution that does not contain information on C_{ab} may explain the poorer performance obtained with bright pixels, for which the importance and variability of the surface reflectance is large. Further inspection shows that the poorer results obtained with bright green pixels are also due to small errors in the co-registration of multispectral bands. These pixels are indeed not only located at the top of canopy, but also on the plant/soil boundaries where the accuracy of the co-registration is the most critical. An error of a few pixels is likely to induce unrealistic VI values at these boundaries, which may have a critical influence on the average VI value. On the other hand, the use of dark green pixels is less affected by errors in the co-registration as these pixels are usually located in the inner part of the canopy and thus surrounded by other green pixels anyway. These results suggest that some improvements are required to allow full exploitation of bright green pixels, hence improving C_{ab} estimation. Three avenues could be explored: (i) improving the co-registration algorithm, (ii), using another multispectral camera technology for which the different wavebands natively overlap, e.g., the one presented by Lee et al. (2014) or (iii) excluding pixels on plant/soil boundaries (this would, however, require a significant increase in spatial resolution to make the number of excluded pixels negligible compared to the total number of bright green pixels).

4.5. Using covariables improves the estimation of canopy biochemistry (CCC, CNC)

The addition of the information on C_{ab} derived from #Avg(VI_GreenPix) to that of $GF_{GREENPIX}$ within the #MLR approach does not significantly improve the estimation of single canopy structure variables such as GF and GAI (Table 10). The $GF_{GREENPIX}$ estimates already provide very accurate GF estimates. The same applies to GAI estimates based on log(1- $GF_{GREENPIX}$) because of the very strong relationship between GAI and GF (Table 5).

Conversely, in the case of CCC estimation, the #GAI.C_{ab} and #MLR approaches substantially outperform the other approaches based on a single input variable (#VI(Avg_Refl), #Avg(VI_AllPix)) (Table 10). In fact, when directly related to CCC, VIs may not simultaneously detect CCC variations due to GAI and C_{ab} with sufficient accuracies. For example, $VARI$ and $NDVI$ are strongly sensitive to GAI (up to $GAI \approx 3.00$) but nearly insensitive to C_{ab} (Table 8), which partly explains the scatters observed for CCC in Figs. 9.b-c. Similarly, CI_{r-e} is more sensitive to C_{ab} than $VARI$ and $NDVI$, but less sensitive to GAI (Table 8). As a result, these three VIs obtain a similar accuracy of 0.19 g/m² for CCC. On the other hand, #GAI.C_{ab} exploits independently the two optimal configurations for estimating the two components of CCC, namely, using $VARI$ and all the pixels of the microplot image for GAI, and using mND_{blue} and only the darkest green pixels for C_{ab}. #GAI.C_{ab} thus makes it possible to accurately capture the two sources of CCC variations, e.g., the variations due to C_{ab} that were not detected with $VARI$ or $NDVI$ alone. This yields a significant 37 % gain in accuracy over #VI(Avg_Refl) and #Avg(VI_AllPix). Note that #GAI.C_{ab} performs slightly better than #MLR since it directly combines the best estimates of GAI and C_{ab} in a multiplicative way, as opposed to #MLR for which the two input variables are combined in an additive way.

The case of CNC appears to be more complex than that of CCC. #GAI.C_{ab} does not bring any improvement as compared to #VI(Avg_Refl) and #Avg(VI_AllPix), while the #MLR approach leads to the best performance (Table 10). In fact, nitrogen does not absorb light at the six wavebands sampled by the camera (Curran, 1989), which means that CNC can mainly be retrieved through its presumed correlation with CCC. Therefore, the strong improvements obtained for C_{ab} and CCC when exploiting the centimeter resolution, do not result in a strong improvement for CNC because CCC and CNC show a poorer correlation for $CNC \geq 5.0$ g/m², as already suggested by Jay et al. (2017b) between different years. The more comprehensive data set used here thus indicates that CCC is generally not an accurate proxy of CNC for large CNC values in sugar beet crops. Actually, a significant amount of the nitrogen uptake is stored in the root for the latest stages (Draycott, 2006), which could explain the loose relationship between leaf nitrogen content and C_{ab} for such stages.

5. Conclusions and perspectives

This study aims to quantify the benefits of centimeter-resolution multispectral imagery as acquired from a UAV for the estimation of GF, GAI, C_{ab}, CCC and CNC in sugar beet crops. Besides testing classical methods (#Avg(VI_AllPix) and #Avg(VI_GreenPix)) that relate each targeted plant trait and the average VI value computed over a particular subset of pixels, we propose several novel methods (#Frac(GreenPix), #GAI.C_{ab} and

#MLR) that exploit the centimeter resolution to improve the estimation of canopy-level variables. #Frac(GreenPix) exploits the GF estimate (denoted $GF_{GREENPIX}$) obtained by thresholding the $VARI$ image to identify the green pixels. $GF_{GREENPIX}$ is shown to be at least as accurate as GF estimates derived from other approaches based on VI values averaged over the microplots, while being less dependent from soil optical properties and variable illumination conditions leading to poor reflectance correction. Further, the logarithmic transformation of $GF_{GREENPIX,}$ $\log(1- GF_{GREENPIX})$, provides the best GAI estimate at least up to $GAI \geq 3.00$. For larger GAI values corresponding to $GF_{GREENPIX} \approx 1$, #Frac(GreenPix) should be combined with another approach exploiting the red-edge and/or near infrared band(s) that should be still sensitive to GAI variations. In the case of C_{ab} estimation, the results show the superiority of mND_{blue} computed over the darkest green pixels (denoted VI_{CAB}), as compared to other approaches using all the pixels of the microplot. By simply multiplying these C_{ab} estimates by the #Frac(GreenPix) GAI estimates, the chlorophyll content at the leaf level can be upscaled to the canopy level, leading to the best CCC estimates (#GAI.C_{ab} approach). Similarly, combining $\log(1- GF_{GREENPIX})$ and VI_{Cab} within a multiple linear regression model (#MLR) leads to the best CNC estimates.

Compared to two standard remote-sensing approaches applied to average microplot reflectances, the centimeter-resolution methods always improve the estimation performance, with a minimum gain of 8 % for GAI and CNC, and maximum gains of 26 and 37 % for C_{ab} and CCC, respectively. It is worth noting here that the centimeter-resolution methods based on $GF_{GREENPIX}$ would have led to even stronger gains if the illumination conditions had strongly varied during the flights (this was not the case here). Since $GF_{GREENPIX}$ and VI_{CAB} are sufficient to retrieve all the five targeted plant traits and can be computed using a low-cost multispectral (or even RGB for $GF_{GREENPIX}$ only) camera, these two variables are promising for important agricultural applications such as precision agriculture and phenotyping. In addition, the methods presented in this study might be useful for the calibration and/or validation of vegetation land products derived from satellite imagery.

Despite the diversity of the data set used in this study, the robustness of the proposed empirical models should be further assessed using a larger and more contrasted data set. Also, because some of the results presented in this paper may be specific to sugar beet crops, they should be re-evaluated for other species. For example, the two $VARI$ thresholds leading to optimal GF and C_{ab} estimates may change with the canopy structure and spatial resolution of the multispectral images. That said, the strong discrimination abilities of $VARI$ suggest that finely tuning these thresholds is not critical and that a unique threshold between 0.05 and 0.25 may be sufficient for most cases if the spatial resolution is fine enough. The accuracy of GAI and C_{ab} estimation should also be confirmed by using direct reference measurements, e.g., as provided using a pigment extraction method for C_{ab}. A variety of other machine learning algorithms (Feilhauer et al., 2015; Verrelst et al., 2016) could be tested to better handle possible non-linearities between $GF_{GREENPIX}$ (or log(1- $GF_{GREENPIX}$)), VI_{CAB} and the targeted variables. Finally, note that exploiting the high-resolution imagery through the $GF_{GREENPIX}$ and VI_{CAB} variables requires a very accurate registration between the several images constituting the multispectral image. Refining the co-registration process thus represents another way of improvement.

Acknowledgments

This work was supported by the French National Research Agency in the framework of the "Investissements d'avenir" programs through AKER (ANR-11-BTBR-0007) and PHENOME (ANR-11-INBS-012). Thanks a lot to Mathieu Hemmerlé for his help in the experiments, and the three reviewers for their valuable comment and recommendations.

References

Aasen, H., Burkart, A., Bolten, A., Bareth, G., 2015. Generating 3D hyperspectral information with lightweight UAV snapshot cameras for vegetation monitoring: From camera calibration to quality assurance. ISPRS J. Photogramm. Remote Sens. 108, 245–259. doi:10.1016/j.isprsjprs.2015.08.002

Andrieu, B., Allirand, J.M., Jaggard, K., 1997. Ground cover and leaf area index of maize and sugar beet crops. Agronomie 17, 315–321.

Araus, J.L., Cairns, J.E., 2014. Field high-throughput phenotyping: The new crop breeding frontier. Trends Plant Sci. 19, 52–61. doi:10.1016/j.tplants.2013.09.008

Baret, F., Buis, S., 2008. Estimating canopy characteristics from remote sensing observations: review of methods and associated problems, in: Liang, S. (Ed.), Advances in Land Remote Sensing: System, Modeling, Inversion and Application. pp. 173–201. doi:10.1007/978-1-4020-6450-0_7

Baret, F., Fourty, T., 1997. Estimation of leaf water content and specific leaf weight from reflectance and transmittance measurements. Agronomie 17, 455–464.

Baret, F., Houlès, V., Guérif, M., 2007. Quantification of plant stress using remote sensing observations and crop models: The case of nitrogen management. J. Exp. Bot. 58, 869–880. doi:10.1093/jxb/erl231

Baret, F., Jacquemoud, S., Guyot, G., Leprieur, C., 1992. Modeled analysis of the biophysical nature of spectral shifts and comparison with information content of broad bands. Remote Sens. Environ. 41, 133–142.

Busemeyer, L., Mentrup, D., Möller, K., Wunder, E., Alheit, K., Hahn, V., Maurer, H.P., Reif, J.C., Würschum, T., Müller, J., 2013. Breedvision—A multi-sensor platform for non-destructive field-based phenotyping in plant breeding. Sensors 13, 2830–2847.

Cerovic, Z.G., Masdoumier, G., Ghozlen, N. Ben, Latouche, G., 2012. A new optical leaf-clip meter for simultaneous non-destructive assessment of leaf chlorophyll and epidermal flavonoids. Physiol. Plant. 146, 251–260. doi:10.1111/j.1399-3054.2012.01639.x

Clevers, J.G.P.., 1997. A simplified approach for yield prediction of sugar beet based on optical remote sensing data. Remote Sens. Environ. 61, 221–228. doi:10.1016/S0034-4257(97)00004-7

Comar, A., Burger, P., de Solan, B., Baret, F., Daumard, F., Hanocq, J.-F., 2012. A semi-automatic system for high throughput phenotyping wheat cultivars in-field conditions: description and first results. Funct. Plant Biol. 39, 914–924. doi:10.1071/FP12065

Croft, H., Chen, J.M., Luo, X., Bartlett, P., Chen, B., Staebler, R.M., 2017. Leaf chlorophyll content as a proxy for leaf photosynthetic capacity. Glob. Chang. Biol. 23, 3513–3524. doi:10.1111/gcb.13599

Curran, P.J., 1989. Remote sensing of foliar chemistry. Remote Sens. Environ. 30, 271–278.

Dash, J., Curran, P.J., 2004. The MERIS terrestrial chlorophyll index. Int. J. Remote Sens. 25, 5403–5413. doi:10.1080/0143116042000274015

Deery, D., Jimenez-Berni, J., Jones, H., Sirault, X., Furbank, R., 2014. Proximal remote sensing buggies and potential applications for field-based phenotyping. Agronomy 4, 349–379.

Demarez, V., Duthoit, S., Baret, F., Weiss, M., Dedieu, G., 2008. Estimation of leaf area and clumping indexes of crops with hemispherical photographs. Agric. For. Meteorol. 148, 644–655. doi:10.1016/j.agrformet.2007.11.015

Domingues Franceschini, M., Bartholomeus, H., van Apeldoorn, D., Suomalainen, J., Kooistra, L., 2017. Intercomparison of Unmanned Aerial Vehicle and Ground-Based Narrow Band Spectrometers Applied to Crop Trait Monitoring in Organic Potato Production. Sensors 17, 1428. doi:10.3390/s17061428

Dong, T., Liu, J., Qian, B., Jing, Q., Croft, H., Chen, J., Wang, J., Huffman, T., Shang, J., Chen, P., 2017. Deriving Maximum Light Use Efficiency from Crop Growth Model and Satellite Data to Improve Crop Biomass Estimation. IEEE J. Sel. Top. Appl. Earth Obs. Remote Sens. 10, 104–117. doi:10.1109/JSTARS.2016.2605303

Dorigo, W. a., 2012. Improving the robustness of cotton status characterisation by radiative transfer model inversion of multi-angular CHRIS/PROBA data. IEEE J. Sel. Top. Appl. Earth Obs. Remote Sens. 5, 18–29. doi:10.1109/JSTARS.2011.2171181

Dorigo, W. a., Zurita-Milla, R., de Wit, a. J.W., Brazile, J., Singh, R., Schaepman, M.E., 2007. A review on reflective remote sensing and data assimilation techniques for enhanced agroecosystem modeling. Int. J. Appl. Earth Obs. Geoinf. 9, 165–193. doi:10.1016/j.jag.2006.05.003

Draycott, A.P., 2006. Sugar beet. Blackwell Publishing Ltd.

Duan, S.B., Li, Z.L., Wu, H., Tang, B.H., Ma, L., Zhao, E., Li, C., 2014. Inversion of the PROSAIL model to estimate leaf area index of maize, potato, and sunflower fields from unmanned aerial vehicle hyperspectral data. Int. J. Appl. Earth Obs. Geoinf. 26, 12–20. doi:10.1016/j.jag.2013.05.007

Dumas, J.B.A., 1831. Procedes de l’analyse organique. Ann. Chim. Phys 47, 198–205.

Feilhauer, H., Asner, G.P., Martin, R.E., 2015. Multi-method ensemble selection of spectral bands related to leaf biochemistry. Remote Sens. Environ. 164, 57–65. doi:10.1016/j.rse.2015.03.033

Feret, J.-B., François, C., Asner, G.P., Gitelson, A. a., Martin, R.E., Bidel, L.P.R., Ustin, S.L., le Maire, G., Jacquemoud, S., 2008. PROSPECT-4 and 5: Advances in the leaf optical properties model separating photosynthetic pigments. Remote Sens. Environ. 112, 3030–3043. doi:10.1016/j.rse.2008.02.012

Féret, J.-B., Gitelson, A.A., Noble, S.D., Jacquemoud, S., 2017. PROSPECT-D: Towards modeling leaf optical properties through a complete lifecycle. Remote Sens. Environ. 193, 204–215. doi:10.1016/j.rse.2017.03.004

Furbank, R.T., Tester, M., 2011. Phenomics - technologies to relieve the phenotyping bottleneck. Trends Plant Sci. 16, 635–644. doi:10.1016/j.tplants.2011.09.005

Gago, J., Douthe, C., Coopman, R.E., Gallego, P.P., Ribas-Carbo, M., Flexas, J., Escalona, J., Medrano, H., 2015. UAVs challenge to assess water stress for sustainable agriculture. Agric. Water Manag. 153, 9–19. doi:10.1016/j.agwat.2015.01.020

Gitelson, A.A., Gritz, Y., Merzlyak, M.N., 2003. Relationships between leaf chlorophyll content and spectral reflectance and algorithms for non-destructive chlorophyll assessment in higher plant leaves. J. Plant Physiol. 160, 271–282. doi:10.1078/0176-1617-00887

Gitelson, A.A., Kaufman, Y.J., Stark, R., Rundquist, D., 2002. Novel algorithms for remote estimation of vegetation fraction. Remote Sens. Environ. 80, 76–87. doi:10.1016/S0034-4257(01)00289-9

Gitelson, A.A., Keydan, G.P., Merzlyak, M.N., 2006a. Three-band model for noninvasive estimation of chlorophyll, carotenoids, and anthocyanin contents in higher plant leaves. Geophys. Res. Lett. 33, 1–6.

doi:10.1029/2006GL026457

Gitelson, A.A., Vina, A., Ciganda, V., Rundquist, D.C., Arkebauer, T.J., 2005. Remote estimation of canopy chlorophyll content in crops. Geophys. Res. Lett. 32, 1–4. doi:10.1029/2005GL022688

Gitelson, A.A., Viña, A., Verma, S.B., Rundquist, D.C., Arkebauer, T.J., Keydan, G., Leavitt, B., Ciganda, V., Burba, G.G., Suyker, A.E., 2006b. Relationship between gross primary production and chlorophyll content in crops: Implications for the synoptic monitoring of vegetation productivity. J. Geophys. Res. Atmos. 111, 1–13. doi:10.1029/2005JD006017

Haboudane, D., Tremblay, N., Miller, J.R., Vigneault, P., 2008. Remote estimation of crop chlorophyll content using spectral indices derived from hyperspectral data. IEEE Trans. Geosci. Remote Sens. 46, 423–436. doi:10.1109/TGRS.2007.904836

Hilker, T., Gitelson, A., Coops, N.C., Hall, F.G., Black, T.A., 2011. Tracking plant physiological properties from multi-angular tower-based remote sensing. Oecologia 165, 865–876.

Houborg, R., McCabe, M.F., Cescatti, A., Gitelson, A.A., 2015. Leaf chlorophyll constraint on model simulated gross primary productivity in agricultural systems. Int. J. Appl. Earth Obs. Geoinf. 43, 160–176. doi:10.1016/j.jag.2015.03.016

Hunt, E.R., Doraiswamy, P.C., McMurtrey, J.E., Daughtry, C.S.T., Perry, E.M., Akhmedov, B., 2012. A visible band index for remote sensing leaf chlorophyll content at the canopy scale. Int. J. Appl. Earth Obs. Geoinf. 21, 103–112. doi:10.1016/j.jag.2012.07.020

Inoue, Y., Guérif, M., Baret, F., Skidmore, A., Gitelson, A., Schlerf, M., Darvishzadeh, R., Olioso, A., 2016. Simple and robust methods for remote sensing of canopy chlorophyll content: a comparative analysis of hyperspectral data for different types of vegetation. Plant. Cell Environ. 2609–2623. doi:10.1111/pce.12815

Inoue, Y., Sakaiya, E., Zhu, Y., Takahashi, W., 2012. Diagnostic mapping of canopy nitrogen content in rice based on hyperspectral measurements. Remote Sens. Environ. 126, 210–221.

doi:10.1016/j.rse.2012.08.026

Jacquemoud, S., Baret, F., 1990. PROSPECT: A model of leaf optical properties spectra. Remote Sens. Environ. 34, 75–91. doi:10.1016/0034-4257(90)90100-Z

Jacquemoud, S., Baret, F., Andrieu, B., Danson, F.M., Jaggard, K., 1995. Extraction of Vegetation Biophysical Parameters by Inversion of the PROSPECT + SAIL Models on Sugar Beet Canopy Reflectance Data. Application to TM and AVIRIS Sensors. Remote Sens. Environ. 52, 163–172.

Jacquemoud, S., Verhoef, W., Baret, F., Bacour, C., Zarco-Tejada, P.J., Asner, G.P., François, C., Ustin, S.L., 2009. PROSPECT+SAIL models: A review of use for vegetation characterization. Remote Sens. Environ. 113, S56–S66. doi:10.1016/j.rse.2008.01.026

Jay, S., Bendoula, R., Hadoux, X., Féret, J.-B., Gorretta, N., 2016. A physically-based model for retrieving foliar biochemistry and leaf orientation using close-range imaging spectroscopy. Remote Sens. Environ. 177, 220–236. doi:http://dx.doi.org/10.1016/j.rse.2016.02.029

Jay, S., Gorretta, N., Morel, J., Maupas, F., Bendoula, R., Rabatel, G., Dutartre, D., Comar, A., Baret, F., 2017a. Estimating leaf chlorophyll content in sugar beet canopies using millimeter- to centimeter-scale reflectance imagery. Remote Sens. Environ. 198, 173–186. doi:10.1016/j.rse.2017.06.008

Jay, S., Maupas, F., Bendoula, R., Gorretta, N., 2017b. Retrieving LAI, chlorophyll and nitrogen contents in sugar beet crops from multi-angular optical remote sensing: Comparison of vegetation indices and PROSAIL inversion for field phenotyping. F. Crop. Res. 210, 33–46. doi:http://dx.doi.org/10.1016/j.fcr.2017.05.005

Jay, S., Rabatel, G., Hadoux, X., Moura, D., Gorretta, N., 2015. In-field crop row phenotyping from 3D modeling performed using Structure from Motion. Comput. Electron. Agric. 110, 70–77. doi:10.1016/j.compag.2014.09.021

Jiang, J., Comar, A., Burger, P., Bancal, P., Weiss, M., Baret, F., 2018. Estimation of leaf traits from reflectance measurements : comparison between methods based on vegetation indices and several versions of the

PROSPECT model. Plant Methods 1–16. doi:10.1186/s13007-018-0291-x

Jin, X., Liu, S., Baret, F., Hemerlé, M., Comar, A., 2017. Estimates of plant density of wheat crops at emergence from very low altitude UAV imagery. Remote Sens. Environ. 198, 105–114. doi:10.1016/j.rse.2017.06.007

Kauth, R.J., Thomas, G.S., 1976. The tasselled cap--a graphic description of the spectral-temporal development of agricultural crops as seen by Landsat, in: Proceedings of the Symposium on Machine Processing of Remotely Sensed Data. pp. 41–51.

Kuusk, A., 1991. The hot spot effect in plant canopy reflectance, in: Photon-Vegetation Interactions. Springer, pp. 139–159.

Lati, R.N., Filin, S., Eizenberg, H., 2013. Estimating plant growth parameters using an energy minimization-based stereovision model. Comput. Electron. Agric. 98, 260–271. doi:10.1016/j.compag.2013.07.012

Launay, M., Guerif, M., 2005. Assimilating remote sensing data into a crop model to improve predictive performance for spatial applications. Agric. Ecosyst. Environ. 111, 321–339. doi:10.1016/j.agee.2005.06.005

Lee, H., Park, S.H., Noh, S.H., Lim, J., Kim, M.S., 2014. Development of a portable 3CCD camera system for multispectral imaging of biological samples. Sensors 14, 20262–20273.

Li, W., Weiss, M., Waldner, F., Defourny, P., Demarez, V., Morin, D., Hagolle, O., Baret, F., 2015. A generic algorithm to estimate LAI, FAPAR and FCOVER variables from SPOT4_HRVIR and landsat sensors: evaluation of the consistency and comparison with ground measurements. Remote Sens. 7, 15494–15516.

McBratney, A., Whelan, B., Ancev, T., Bouma, J., 2005. Future directions of precision agriculture. Precis. Agric. 6, 7–23.

Moorthy, I., Miller, J.R., Noland, T.L., 2008. Estimating chlorophyll concentration in conifer needles with hyperspectral data: An assessment at the needle and canopy level. Remote Sens. Environ. 112, 2824–2838. doi:10.1016/j.rse.2008.01.013

Nilson, T., 1971. A theoretical analysis of the frequency of gaps in plant stands. Agric. Meteorol. 8, 25–38.

Rabatel, G., Labbé, S., 2016. Registration of visible and near infrared unmanned aerial vehicle images based on Fourier-Mellin transform. Precis. Agric. 17, 564–587.

Rouse, J.W., Hass, R.H., Schell, J.A., Deering, D.W., 1973. Monitoring vegetation systems in the great plains with ERTS. Third Earth Resour. Technol. Satell. Symp. 1, 309–317. doi:citeulike-article-id:12009708

Sankaran, S., Khot, L.R., Espinoza, C.Z., Jarolmasjed, S., Sathuvalli, V.R., Vandemark, G.J., Miklas, P.N., Carter, A.H., Pumphrey, M.O., Knowles, R.R.N., Pavek, M.J., 2015. Low-altitude, high-resolution aerial imaging systems for row and field crop phenotyping: A review. Eur. J. Agron. 70, 112–123. doi:10.1016/j.eja.2015.07.004

Schlemmer, M., Gitelson, a., Schepers, J., Ferguson, R., Peng, Y., Shanahan, J., Rundquist, D., 2013. Remote estimation of nitrogen and chlorophyll contents in maize at leaf and canopy levels. Int. J. Appl. Earth Obs. Geoinf. 25, 47–54. doi:10.1016/j.jag.2013.04.003

Steven, M., Malthus, T., Baret, F., 2015. Toward Standardization of Vegetation Indices, in: Prasad S. Thenkabail (Ed.), Remotely Sensed Data Characterization, Classification, and Accuracies, Remote Sensing Handbook. CRC Press, pp. 175–194. doi:doi:10.1201/b19294-13

Van Der Meij, B., Kooistra, L., Suomalainen, J., Barel, J.M., De Deyn, G.B., 2017. Remote sensing of plant trait responses to field-based plant-soil feedback using UAV-based optical sensors. Biogeosciences 14, 733–749. doi:10.5194/bg-14-733-2017

Vapnik, V.N., Vapnik, V., 1998. Statistical learning theory. Wiley New York.

Verger, A., Baret, F., Camacho, F., 2011. Optimal modalities for radiative transfer-neural network estimation of canopy biophysical characteristics: Evaluation over an agricultural area with CHRIS/PROBA observations. Remote Sens. Environ. 115, 415–426.

Verger, A., Vigneau, N., Chéron, C., Gilliot, J.M., Comar, A., Baret, F., 2014. Green area index from an unmanned aerial system over wheat and rapeseed crops. Remote Sens. Environ. 152, 654–664. doi:10.1016/j.rse.2014.06.006

Verhoef, W., 1998. Theory of radiative transfer models applied in optical remote sensing of vegetation canopies. Wageningen Agricultural University.

Verhoef, W., 1985. Earth observation modeling based on layer scattering matrices. Remote Sens. Environ. 17, 165–178.

Verhoef, W., 1984. Light scattering by leaf layers with application to canopy reflectance modeling: The SAIL model. Remote Sens. Environ. 16, 125–141. doi:10.1016/0034-4257(84)90057-9

Verrelst, J., Rivera, J.P., Gitelson, A., Delegido, J., Moreno, J., Camps-Valls, G., 2016. Spectral band selection for vegetation properties retrieval using Gaussian processes regression. Int. J. Appl. Earth Obs. Geoinf. 52, 554–567. doi:10.1016/j.jag.2016.07.016

Weiss, M., Baret, F., Leroy, M., Hautecoeur, O., Bacour, C., Prevol, L., Bruguier, N., 2002. Validation of neural net techniques to estimate canopy biophysical variables from remote sensing data. Agronomie 22, 547–554.

Weiss, M., Baret, F., Smith, G.J., Jonckheere, I., Coppin, P., 2004. Review of methods for in situ leaf area index (LAI) determination Part II. Estimation of LAI, errors and sampling. Agric. For. Meteorol. 121, 37–53. doi:10.1016/j.agrformet.2003.08.001

Woebbecke, D.M., Meyer, G.E., Von Bargen, K., Mortensen, D.A., 1995. Color Indices for Weed Identification Under Various Soil, Residue, and Lighting Conditions. Trans. ASAE 38, 259. doi:https://doi.org/10.13031/2013.27838

Yang, G., Liu, J., Zhao, C., Li, Z., Huang, Y., Yu, H., Xu, B., Yang, X., Zhu, D., Zhang, X., Zhang, R., Feng, H., Zhao, X., Li, Z., Li, H., Yang, H., 2017. Unmanned Aerial Vehicle Remote Sensing for Field-Based Crop Phenotyping: Current Status and Perspectives. Front. Plant Sci. 8. doi:10.3389/fpls.2017.01111

Zaman-Allah, M., Vergara, O., Araus, J.L., Tarekegne, A., Magorokosho, C., Zarco-Tejada, P.J., Hornero, A., Albà, A.H., Das, B., Craufurd, P., Olsen, M., Prasanna, B.M., Cairns, J., 2015. Unmanned aerial platform-based multi-spectral imaging for field phenotyping of maize. Plant Methods 11, 35. doi:10.1186/s13007-015-0078-2

Zarco-Tejada, P.., Miller, J.., Morales, A., Berjón, A., Agüera, J., 2004. Hyperspectral indices and model simulation for chlorophyll estimation in open-canopy tree crops. Remote Sens. Environ. 90, 463–476. doi:10.1016/j.rse.2004.01.017

Zarco-Tejada, P.J., Guillén-Climent, M.L., Hernández-Clemente, R., Catalina, A., González, M.R., Martín, P., 2013. Estimating leaf carotenoid content in vineyards using high resolution hyperspectral imagery acquired from an unmanned aerial vehicle (UAV). Agric. For. Meteorol. 171, 281–294. doi:10.1016/j.agrformet.2012.12.013

Zarco-Tejada, P.J., Miller, J.R., Noland, T.L., Mohammed, G.H., Sampson, P.H., 2001. Scaling-up and model inversion methods with narrowband optical indices for chlorophyll content estimation in closed forest canopies with hyperspectral data. IEEE Trans. Geosci. Remote Sens. 39, 1491–1507. doi:10.1109/36.934080

Zhang, C., Kovacs, J.M., 2012. The application of small unmanned aerial systems for precision agriculture: a review. Precis. Agric. 13, 693–712.

Zhou, X., Zheng, H.B., Xu, X.Q., He, J.Y., Ge, X.K., Yao, X., Cheng, T., Zhu, Y., Cao, W.X., Tian, Y.C., 2017. Predicting grain yield in rice using multi-temporal vegetation indices from UAV-based multispectral and digital imagery. ISPRS J. Photogramm. Remote Sens. 130, 246–255. doi:10.1016/j.isprsjprs.2017.05.003